GEOLOGIC REPORT TO ACCOMPANY THE GEOLOGIC MAP OF THE HAINES-TAKSHANUK MOUNTAINS-CHILKAT PENINSULA AREA, SOUTHEAST ALASKA

Martin C. Larsen, Sean P. Regan, Robert J. Gillis, Jillian A. Nicolazzo, Margaret M. Darrow, Katharine F. Bull, Sandra L. Walser, and Conner M. Truskowski

Preliminary Interpretive Report 2025-4B

DGGS geologist Jillian Nicolazzo conducting surficial mapping in the alpine of the Takshanuk Mountains

This publication is PRELIMINARY in nature and meant to allow rapid release of field observations or initial interpretations of geology or analytical data. It has undergone limited peer review but does not necessarily conform to DGGS editorial standards. Interpretations or conclusions contained in this publication are subject to change.

2025
STATE OF ALASKA
DEPARTMENT OF NATURAL RESOURCES
DIVISION OF GEOLOGICAL & GEOPHYSICAL SURVEYS

STATE OF ALASKA
Mike Dunleavy, Governor

DEPARTMENT OF NATURAL RESOURCES
John Crowther, Acting Commissioner

DIVISION OF GEOLOGICAL & GEOPHYSICAL SURVEYS
Erin A. Campbell, State Geologist & Director

Publications produced by the Division of Geological & Geophysical Surveys are available to download from the DGGS website (dggs.alaska.gov). Publications on hard-copy or digital media can be examined or purchased in the Fairbanks office:

Alaska Division of Geological & Geophysical Surveys (DGGS)
3354 College Road | Fairbanks, Alaska 99709-3707
Phone: 907.451.5010 | Fax 907.451.5050
dggspubs@alaska.gov | dggs.alaska.gov

DGGS publications are also available at:

Alaska State Library, Historical
Collections & Talking Book Center
395 Whittier Street
Juneau, Alaska 99801

Alaska Resource Library and
Information Services (ARLIS)
3150 C Street, Suite 100
Anchorage, Alaska 99503

Suggested citation:
Larsen, M.C., Regan, S.P., Gillis, R.J., Nicolazzo, J.A., Darrow, M.M., Bull, K.F., Walser, S.L., and Truskowski, C.M., 2025, Geologic Report to Accompany the Geologic Map of the Haines-Takshanuk Mountains-Chilkat Peninsula area, Southeast Alaska: Alaska Division of Geological & Geophysical Surveys Preliminary Interpretive Report 2024-9B, 45 p.
https://doi.org/10.14509/31419

GEOLOGIC REPORT TO ACCOMPANY THE GEOLOGIC MAP OF THE HAINES-TAKSHANUK MOUNTAINS-CHILKAT PENINSULA AREA, SOUTHEAST ALASKA

Martin C. Larsen[2], Sean P. Regan[3], Robert J. Gillis[1], Jillian A. Nicolazzo[1], Margaret M. Darrow[4], Katharine F. Bull[2], Sandra L. Walser[1], and Conner M. Truskowski[1]

INTRODUCTION

In response to the deadly December 2, 2020, landslide in Haines, Alaska, Alaska's Geologic Mapping Advisory Board endorsed a STATEMAP-funded project to conduct geologic mapping in the Haines-Takshanuk Mountains-Chilkat Peninsula area of Southeast Alaska. The approximately 777-square-kilometer map area includes portions of the Skagway A-1, A-2, B-1, B-2, and B-3 15-minute quadrangles (fig1). This geologic report provides unit descriptions and supporting information to accompany a 1:50,000-scale surficial and bedrock geologic map (Larsen and others, 2025), hereafter referred to as sheet 1. Sheet 1 provide data to support the systematic evaluation of landslides and unstable slopes in the area and to help answer outstanding research questions in the northern Cordillera.

This project describes the distribution of unconsolidated geologic deposits, identifies local geologic hazards, and provides information about the engineering properties of common surficial- and bedrock-geologic materials. This mapping will be helpful for proactive planning, mitigation, and emergency response in and around this high-risk community. While our primary goal was to produce a new geologic map of the area, we also addressed important outstanding questions about the region's tectonic history by conducting targeted bedrock mapping and structural studies. As such, we leaned heavily on previous geologic mapping by Redman and others (1984), Gilbert and others (1987), and Gilbert (1988). The new bedrock mapping revises these earlier publications by providing new data about the Chatham Strait fault system, Coast shear zone (CSZ), and Coast Plutonic Complex. New petrologic and geochemical analyses of samples collected across much of the study area improve the characterization of bedrock units. However, much work remains to resolve the magmatic and mineralization history of the region.

We mapped the geology of the area through a combination of field observations and interpretation of lidar data and aerial imagery. Geologic units were defined based on our field observations and analysis of samples collected from more than 550 stations. Ground observations were conducted by helicopter- and boat-supported teams of scientists from the Alaska Division of Geological & Geophysical Surveys (DGGS) and the University of Alaska Fairbanks (UAF). While in the field, we documented the morphology and material characteristics of landforms, observed and sampled material from soil test pits, collected

[1] Alaska Division of Geological & Geophysical Surveys, 3354 College Road, Fairbanks, AK 99709

[2] *Formerly* Alaska Division of Geological & Geophysical Surveys, 3354 College Road, Fairbanks, AK 99709

[3] Department of Geosciences and Geophysical Institute, University of Alaska Fairbanks, P.O. Box 755980, Fairbanks, AK 99775

[4] Department of Civil, Geological, and Environmental Engineering, University of Alaska Fairbanks, P.O. Box 755900, Fairbanks, AK 99775

structural data from rock outcrops, conducted Schmidt Hammer tests, and collected rock samples for thin section, major oxide, and trace element analyses. Organic samples were also collected for radiocarbon dating.

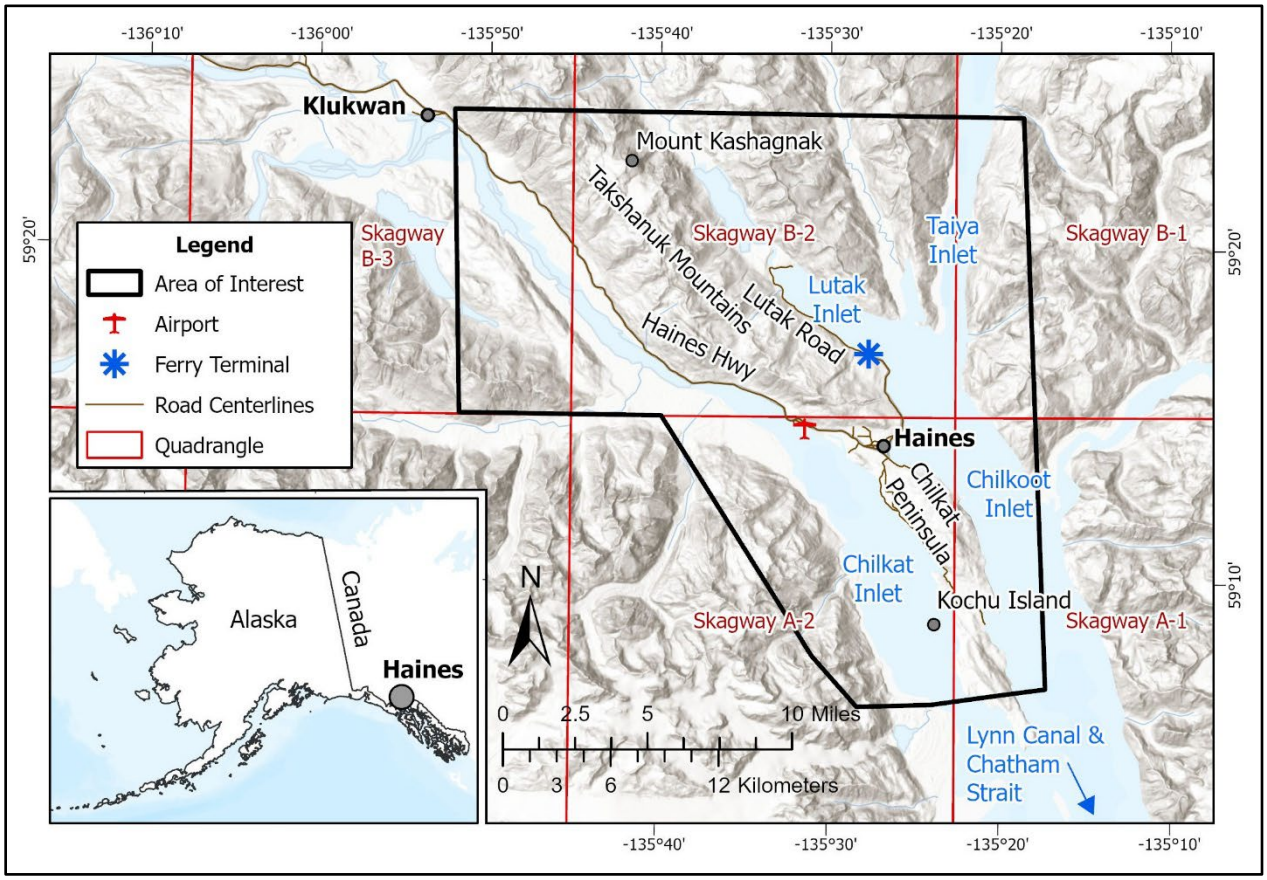

Figure 1. Map showing the area of interest, major infrastructure, and USGS quadrangles.

REGIONAL FRAMEWORK AND GEOLOGY

The bedrock-geologic framework of this area includes the Coast Plutonic Complex and other rock packages cut and deformed by the Chatham Strait fault system and CSZ. The exhumed roots of the Coast Plutonic Complex and associated metamorphic rocks that comprise most of the proposed map area extend for more than 1,700 km from Southeast Alaska and Yukon Territory, Canada, to northern Washington (Gehrels and others, 2009) and record nearly 110 Ma of subduction along the northwest margin of North America beginning after ca. 160 Ma until about 50 Ma (Gehrels and others, 2009). This belt is bound to the southwest, for most of its length, by the CSZ. This highly strained, poly-deformed metamorphic ribbon was principally responsible for exhumation of the Coast Plutonic Complex from depths of up to 25 km (Crawford and others, 1987). The CSZ is a relatively late-stage feature in the construction of the Coast Plutonic Complex and hosts a syn-kinematic Paleogene sill complex up to 10 km wide (the "Great Tonalite Sill" of Ingram and Hutton [1994]). These regional

tectonic relations are dissected in the proposed map area by the Chatham Strait fault—a composite structure that is inferred to transfer slip from the present-day continental transform margin into interior continental Alaska via the Paleogene-to-modern Denali fault system (Hudson and others, 1982).

The morphology of the region broadly reflects the underlying geologic structures but has been greatly modified by Pleistocene glaciation. During the Last Glacial Maximum, this region was blanketed by glaciers that coalesced to form the Cordilleran ice sheet (Carrara and others, 2007; Kaufman and others, 2011), including a glacier that occupied Lynn Canal (Brothers and others, 2018). This large glacier filled the valley and scoured Lynn Canal to bedrock (Brothers and others, 2018). Radiometric dating (^{10}Be and ^{14}C) suggests the Cordilleran ice sheet reached its maximum extent between ca. 20,000 and ca. 17,000 cal. yr B.P. (Lesnek and others, 2018). Fjords and straits were deglaciated by ca. 14,900 cal. yr B.P., and Cordilleran ice sheet margins transitioned to being primarily land-terminating (Lesnek and others, 2020). Small, independent, remnant ice caps may have persisted in high-elevation areas until the early Holocene (Lesnek and others, 2020), although the history of these glaciers remains poorly constrained.

The Haines area currently experiences glacial isostatic adjustment due to loss of ice formed during the Little Ice Age in the Glacier Bay area to the west. Modern isostatic adjustment rates—determined using global positioning system geodetic techniques—are as high as 20 mm/yr, and adjustment is expected to continue for several hundred years (Motyka and others, 2007). This rate of uplift corresponds with suggestions by Yehle and Lemke (1972), who, using tidal records from the early to mid-twentieth century, determined a rate of 22.6 mm/yr. In the project area, glacier-scoured mountains rise steeply from the sea to ~1,645 m at slopes up to 88 degrees. Slopes may be unstable due to oversteepening from glacial erosion and subsequent debuttressing from glacial ice (Evans and Clague, 1999).

STUDY 1: SURFICIAL GEOLOGIC STUDIES

Soil Strength Testing

During geologic mapping fieldwork, soil samples were collected from 24 representative sites to support slope stability analysis. Laboratory testing included moisture content, sieve analysis, Atterberg limits, hydrometer readings, specific gravity, and radiocarbon ages for selected samples (Nicolazzo and others, 2024a). Most samples were granular and classified as sand or silty sand using the Unified Soil Classification System (Nicolazzo and others, 2024a). Two samples were classified as silty clay, with approximately 49 percent sand and gravel content. The overall lack of clay in samples collected across the area suggests that most soils are non-cohesive; therefore, their shear strength is derived from internal friction rather than cohesion.

Surficial deposits on slopes steeper than their internal friction angle are more susceptible to slope instability and erosion, particularly in areas lacking vegetative cover. Many of the slope failures triggered by the December 2020 weather event originated in granular soils along road cuts or steep drainage channels, suggesting a correlation between slope instability and the presence of granular soils on steep terrain.

Radiocarbon Results

We obtained radiocarbon ages for five samples collected within the study area (Nicolazzo and others, 2024a, table 1). A sample of marine shells from station 23MMD029B yielded an age of 12,739±140 yr B.P., which can be used to refine uplift rate estimates for the Haines area (e.g., Darrow and others [2022]). A second sample, collected from the left flank of a recent debris flow on the left bank of an incised channel at station 23MMD012, exposed older debris flow deposits and returned an age of 2,251±95 yr B.P. This suggests that debris flow activity has been ongoing since the Last Glacial Maximum and subsequent glacial isostatic adjustment. The three remaining radiocarbon dates (stations 23MMD021, 23MMD022, and 23MMD025; 304±26 yr B.P., 230±84 yr B.P., and <250 yr B.P., respectively) indicate the historically active and dynamic nature of alluvial fans built by channels draining Mount Ripinski.

Table 1. Radiocarbon age results (Nicolazzo and others [2024a]).

DGGS Sample ID	Lab ID[1]	Material Analyzed	^{14}C Age (yr B.P.)[2]	Sample Depth (cm)	Sample Locality Description
23MMD012	Beta - 691376	Organics in a well-graded sand with silt	2,251±95	50	Left flank of a debris flow
23MMD021	Beta - 691377	Organics in a poorly graded sand with gravel	304±26	200	Alluvial fan covering uplifted marine deposits; exposed in gravel pit off Lutak Road
23MMD022	Beta - 691378	Woody debris	230±84	70	Alluvial fan covering uplifted marine deposits; exposed in gravel pit off Lutak Road
23MMD025	Beta - 691381	Organics in a poorly graded sand with gravel	<250	115	Upper portions of the alluvial fan deposits; exposed in gravel pit off Lutak Road
23MMD029B	Beta - 691382	Marine bivalve	12,739±140	420	Cut slope of private driveway, sample obtained from uplifted marine deposit

[1] All conventional radiocarbon ages were determined by Beta Analytic Testing Laboratory. Calibrated radiocarbon ages were determined using the CALIB Rev 8.1.0 Program using INTCAL20 Calibration Curve for terrestrial samples and the MARINE20 Calibration Curve for shells.

[2] Age in ^{14}C yr B.P. is conventional age in years before A.D. 1950 with quoted laboratory counting error of one standard deviation.

STUDY 2: BRITTLE STRUCTURAL ANALYSIS AND ITS IMPLICATIONS FOR LARGE-SCALE DEXTRAL TRANSLATION ALONG THE CHATHAM STRAIT FAULT

The Chatham Strait fault (CSF) is a north–northwest-trending regional structure that is thought to link with the eastern Denali fault to the northwest of the map area, to transfer right-lateral slip from the Pacific plate boundary into Interior Alaska (fig. 2A; Hudson and others, 1982). The 150 km of dextral motion estimated on the CSF is inferred from laterally separated Paleozoic and early Mesozoic bedrock and middle-to-late Oligocene Admiralty Island Volcanics across the Chatham Strait (figs. 1 and 2A; Lathram, 1964; Ford and others, 1996). Contrasts between more deeply seated plutonic rocks exposed on Baranoff Island to the southwest with respect to volcanic rocks deposited on the surface of Admiralty Island to the northeast (fig. 2A) also suggest several kilometers of up-to-the southwest throw across the CSF since the Miocene (Loney and others, 1967). However, most of the >400 km length of the CSF is hidden beneath Chatham Strait and Lynn Canal (fig. 1), hampering detailed structural studies of its geometry and slip history. In the map area, the CSF transitions into a subaerial system where it branches northward into the Chilkat, Lutak Inlet, Ferebee, and Taiya Inlet faults (fig. 2B; Redman and others, 1984). These fault splays divide bedrock highlands into the Chilkat, Chilkoot, and Ferebee blocks (fig. 2B; Redman and others, 1984) and record information about the structural character of the bounding faults.

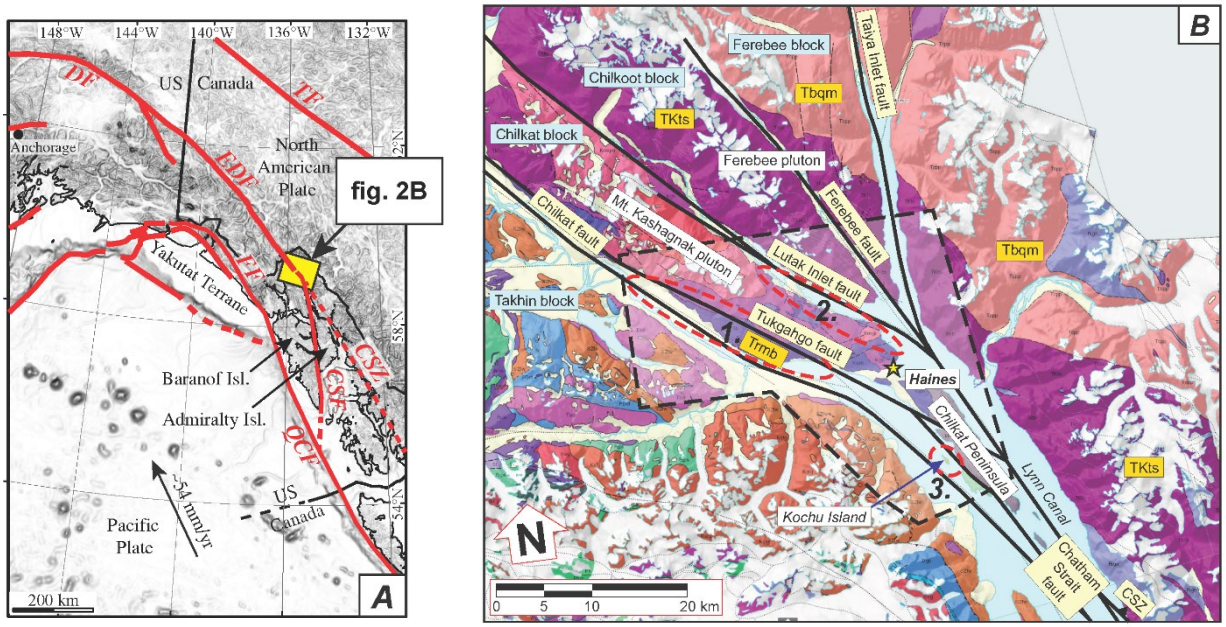

Figure 2. A. Regional tectonic map of southern Alaska and far western Canada showing important fault linkages. QC F= Queen Charlotte fault, CSF = Chatham Strait fault, CSZ = Coast Shear Zone, FF = Fair weather fault, EDF = eastern Denali fault, DF = Denali fault, TF = Tintina fault (modified from Brothers and others, 2018). **B.** Generalized geologic map of the greater Haines area showing major faults, tectonic features, and locations specific to the map area and referred to in the text. See "Description of Map Units" section and Sheet 1 for additional information. Dashed red ovals encompass locations of structural domains discussed below. CSZ = Coast Shear Zone. Rock units in the southwest corner of the map figure consist of principally Proterozoic and Paleozoic metamorphic rocks intruded by Early to Middle Cretaceous and Paleogene granitoids not discussed in topical studies reported herein (see plate 1). Adapted from Wilson and others, 2015.

To improve constraints on CSF geometry and slip, 271 fault plane measurements were collected—most from roadcuts adjacent to Chilkat and Lutak Inlet strands of the CSF (fig. 3A). Kamb-contoured poles to planes produce local maxima that define three principal fault sets at azimuth/plunge 090/45 (set A), 043/35 (set B), and 219/40 (set C; fig. 3B). Set A is composed of south-striking faults (n=51) with moderate dips and constitutes the principal set (figs. 3A and 3B). Moderately to steeply dipping set B (n=38) and moderately dipping set C (n=28) strike to the southeast and northwest, respectively, but with nearly identical trends (figs. 3A and 3B). Brittle fault slip lineations variably plunge steeply to shallowly for all three sets, although most commonly exhibit steep to moderate plunges (fig. 3A). A preliminary kinematic fault analysis yielded complete unidirectional slip indicators (n=145; figs. 4A–E) to define the slip mode(s) of the fault system, quantify the associated strain axes, and test for multiple generations of deformation. The methodology and results are discussed below.

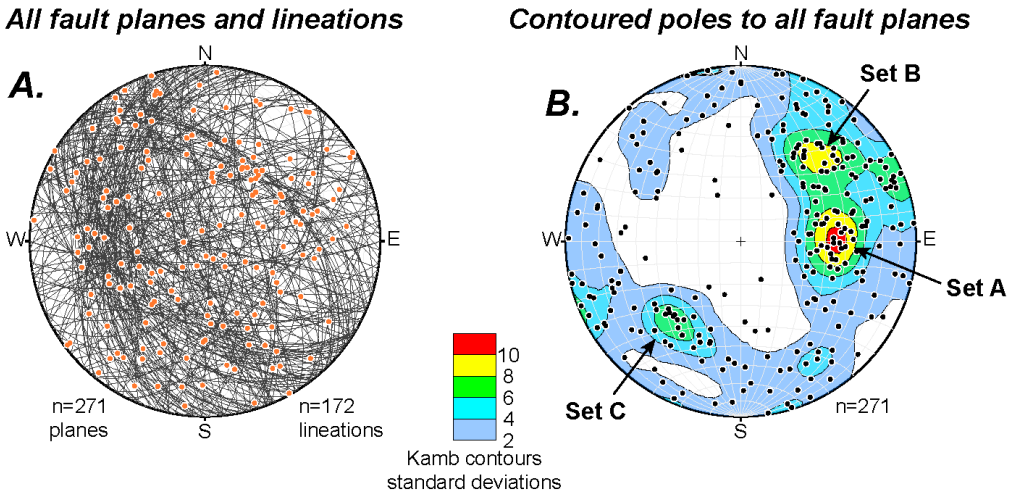

Figure 3. Stereographic projections of all measured map area faults and lineations. **A.** Fault planes (gray arcs) and lineations (orange dots). **B.** Contoured poles to fault planes highlighting main fault sets.

Methods

The kinematic analysis was conducted using Faultkin software version 10 (Marrett and Allmendinger, 1990; Allmendinger and others, 2012), to calculate the principal axes of the incremental strain tensor for each fault based on its orientation and slip direction (fig. 4A; Arthaud, 1969). Fault domains were qualitatively defined based on relative position to mapped faults; for instance, outcrops arrayed parallel to the Chilkat strand of the CSF along the Haines Road fig. 2B). Each domain was analyzed for kinematic compatibility (i.e., faults whose slip directions are consistent with a common stressor) using the P & T dihedra method of Angelier and Mechler (1977). A subset was created of the maximum number of kinematically compatible faults in a domain, assuming their deformation was the result of a common event. The incompatible faults were removed and tested for internal compatibility, potentially resulting from a second deformation. A linked Bingham calculation (Bingham, 1974) on each collection of strain axes was used to estimate the strain axes orientations for

each fault set or subset. Fault plane solutions were generated from the linked Bingham axes orientations for easy visualization of fault domain movement.

Results

Domain 1, Haines Rd faults, (figs. 4B and 4C) is confined between the northwest-trending Chilkat and Tukgahgo faults and contains all three principal fault sets (fig. 3B). Data for 118 faults that range in length from a few meters to several 10s of meters or more were collected from discontinuous roadcut outcrops of Triassic basalt (unit Trmb) along a 16 km stretch of the Haines Highway (fig. 2). The data suggest that slip surfaces record two distinct deformations. The maximum number of kinematically compatible faults (n=94 of 118) produce a subhorizontal northeast-oriented maximum shortening axis and subvertical elongation axis consistent with reverse oblique slip common to all three fault sets (fig. 4B). The remaining, incompatible subset (n=24 of 118) consists mainly of faults in sets A and B but no faults in set C (fig. 3B). The maximum shortening and elongation axes of the residual subset (fig. 4C) are oriented subhorizontally and favor sinistral strike slip on set A and set B faults, with the southeast maximum shortening direction nearly orthogonal to that of the maximum compatible subset (fig. 4B). P & T dihedral analysis of the residual subset reveals that faults comprising this group are largely internally compatible (22 of 24 faults; fig. 4C), suggesting kinematic congruence and reactivation of set A and set B faults from a second deformation, although the relative timing of the two deformations is unconstrained.

Domain 2, Lutak Rd faults (n=15) (fig. 4D) were collected from discontinuous roadcut outcrops (of units Trmb, Kum, and Kkhd) off Lutak Road along Chilkoot and Lutak inlets due east of the Lutak Inlet strand of the CSF (fig. 2). The domain consists mainly of set B and set C faults (fig 3B) that are nearly all kinematically compatible (14 of 15; fig. 4D) and produce Bingham axes that are nearly identical to those of domain 1 (fig. 4B), suggesting that northwest-oriented reverse faults from both domains were deformed by a common state of northeast shortening.

Domain 3, Kootznahoo faults, (fig. 4E) on Kochu Island, located in Chilkat Inlet west of Chilkat Peninsula (fig. 2), consists only of set C (fig 3B) reverse faults (n=4; fig. 4E). The island is situated between an imprecisely mapped strand of the CSF to the west that bifurcates northward into the Chilkat and Tukgahgo faults (Wilson and others, 2015) and a north-northwest-trending fault to the east on Chilkat Peninsula, that separates middle Cretaceous Gravina belt turbidites (Kgb) from Triassic basalts of unit Trmb. Domain 3 faults produce comparable maximum shortening axes as domain 1 and 2 reverse faults and are significant because they cut westward-tilted Eocene Kootznahoo Formation strata. Thus, they established a maximum age of northeast contraction at this location.

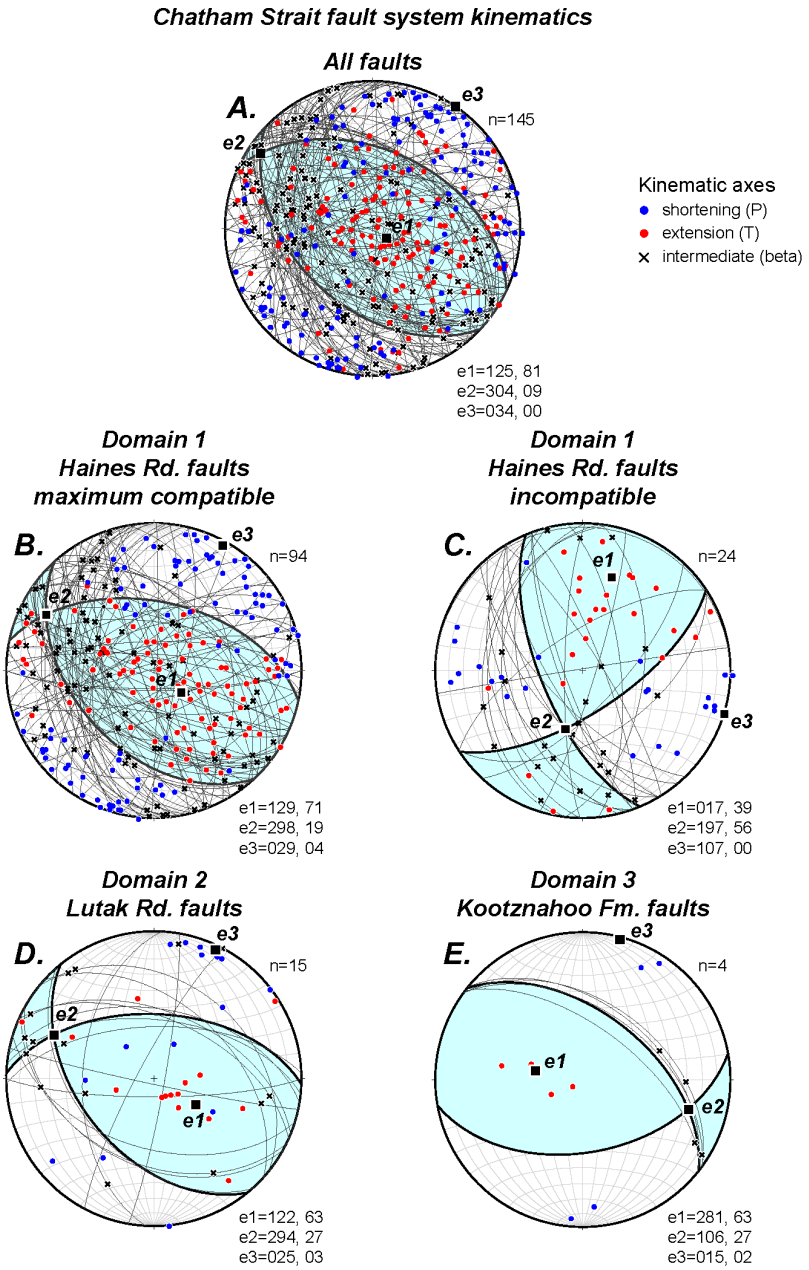

Figure 4. Stereographic projections of kinematic analyses (e1–e3) for three fault domains showing maximum extension (T; red circles), shortening (P; blue circles), and intermediate (beta; black x symbols) strain axes for each fault surface (gray arcs). Black numbered squares are linked Bingham principal strain axes calculated for each domain or domain subset: e1 = maximum extension axis, e2 = the intermediate strain axis, and e3 = the axis of maximum contraction.

Summary

Preliminary results from fault kinematic studies within the map area indicate that rocks adjacent to CSF strands have been deformed contractionally by northeast-directed, fault-

normal shortening with only minor evidence of dextral strike slip. The three domains defined above (fig 4) encompass 95 percent of all faults measured in the map area, with northwest-trending reverse faults (sets B and C) constituting 56 percent of the major fault sets. The trends of sets B and C (313° and 309°, respectively) are nearly identical to the mapped trends of the Chilkat, Lutak Inlet, and Tukgahgo faults (approximately 310°) (fig. 2), suggesting that the strands of the CSF may also be contractional.

An interesting result from the kinematic analysis is that a second, perhaps earlier deformation recorded in domain 1 favors left-lateral slip along northwest- and north-trending faults rather than right-lateral motion as anticipated from northwest directed Pacific Plate motion with respect to continental North America (fig. 2A). Gehrels and others (2009) summarize evidence of large-magnitude (>800 km) Early Cretaceous sinistral strike slip from the Coast Mountains batholith, including individual left-lateral faults in a comparable position to the map area on the western flank of the Coast Mountains to the southeast in British Columbia (Chardon and others, 1999). If the left-lateral fault subset is a vestige of the Early Cretaceous event, then the northwest-trending contractional faults may have inherited the earlier fabric and destroyed much of the sinistral-slip history during their reactivation. Domain 3 faults cut west-tilted Kootznahoo Formation strata, tentatively constraining northeast contraction to Eocene or later.

However, the high obliquity of Pacific basin plate motion with respect to North America since the Late Cretaceous (Doubrovine and Tarduno, 2008) seemingly presents challenges to reconciling northeast contraction constrained by fault slip data from the map area with a tectonic framework that favors large-magnitude dextral strike slip and northward coastwise terrane translation. An end-member interpretation is that motion has been largely partitioned along the CSF into distinct strike-slip and contractional components (e.g., Tikoff and Teyssier, 1994; Teyssier and others, 1995), where the main strands of the system (e.g., Chilkat and Lutak Inlet strands) principally accommodate the strike-slip fraction and the intervening bedrock highlands chiefly the contractional fraction. In this scenario, the small component of dextral slip recorded for each domain would reflect imperfect partitioning at the regional fault interfaces. In another end member, the CSF trends in a more northerly direction than its northwest-trending splay faults for most of its length (~340° vs. ~310°, respectively), which results in a 30° restraining bend at their junction (fig. 2B) and favors dextral contraction on the northwest-trending strands. Further work is required to distinguish between the end-member models.

Ongoing analyses are anticipated to cast additional light on outstanding questions. For instance, pending low-temperature thermochronologic analyses of samples collected from the bedrock highlands across the CSF splays will improve constraints on the timing and rate of potential restraining-bend evolution, and thus inception, of CSF slip. Additionally, Kootznahoo Formation conglomerate in the map area and a similar conglomerate that crops out near Berners Bay (Jualin formation of Redman [1984]) approximately 40 km to the southeast of the mapped area are currently being evaluated as tie points across potential coastal dextral faults that may feed slip into the CSF, perhaps accounting for some of the slip deficit recognized between the CSF and Denali fault systems.

STUDY 3: UNIT TKts—TONALITE SILL

"The Great Tonalite Sill" of Ingram and Hutton (1994) is a ~1,400-km-long composite intrusive complex ranging from 10 to 18 km wide in plan view that parallels the strike of the Coast Mountains orogen (Gehrels and others, 2009; fig. 2). Within our map area, positioned along the northern portion of the Coast Mountains in Southeast Alaska, map unit **TKts** corresponds to the northern limit of the tonalite sill complex (fig. 2 and sheet 1). Mapping was conducted to identify the continuity of this important intrusive unit, characterize its contacts, and document deformational features. It is interleaved with metamorphic rocks of (Unit MzPzgm), particularly in the eastern limit in Unit TKts. The eastern margin of TKts and MzPzgm is an intrusive contact with younger tonalitic rocks (Tbqm) of the axial portion of the Coast Mountains batholith (Gehrels et al., 2009).

TKts Extent

Unit TKts is predominantly a medium-grained hornblende–biotite granodiorite that extends from Lutak Inlet eastward (fig. 2) but is not exposed to the west of the Lutak inlet fault. We interpret the tonalite sill to be in fault contact with rocks to the west, similar to interpretations by Redman and others (1984). Redman and others (1984) referred to intrusive rocks in the Chilkoot and Ferebee structural blocks east of Lutak Inlet as the "Ferebee Pluton" (fig. 2) and preliminarily correlated it to tonalite sill plutonism (Ingram and Hutton, 1994). New mapping shows lithologic continuity across Taiya Inlet from the Ferebee Pluton on the northwest to the tonalite sill complex recognized to the southeast, indicating that the Ferebee pluton is the northwestern extension of the tonalite sill complex, which is truncated along its southwestern margin by northwest-oriented brittle faults (the Lutak Inlet and associated faults to the southeast). The western margin of the tonalite sill contains abundant screens of Paleozoic to early Mesozoic gneiss and migmatite (unit MzPzgm). In a location outside of the map area (station 23SPR149, Truskowski and others, 2024b), a complex intrusive contact is preserved between metagabbroic and dioritic rocks (unit TKts?) and leucogranite (unit Tgd?), where networks of dikes and sills (unit Tgd?) have intruded host rock in a polygonal pattern. This leucogranite may not be related to unit Tbqm and may instead be the youngest generation of TKts magmatism near the structural top of the intrusion (sheet 1). In the northeast corner of the map area (sheet 1), a minor fault in Taiya Inlet offsets the Tbqm–MzPzgm contact with ~2 km of strike slip separation.

Foliation in Unit TKts is moderately dipping to the east and variably deformed, with a strong foliation and lineation along its western flank. Southeast of the map area, unit TKts intrudes and shares a deformational fabric with supracrustal rocks of the Yukon–Tanana and Taku terranes of the western metamorphic belt (Himmelberg and others, 1991; Gehrels and others, 2009; Regan and others, 2024), which collectively preserve a moderately eastward-dipping gneissosity and (or) cleavage. Similar fabrics were recognized in the map area (fig. 5). This fabric dissipates with structural height (eastward and with elevation) within unit TKts. In conjunction with a general decrease in subsolidus fabric intensity, unit TKts contains numerous xenoliths ranging in scale from meters to km that increase in abundance with structural height and include amphibolite (fig 5C, calc-silicate gneisses, and quartzofeldspathic migmatitic gneisses (unit MzPzgm). Gneissosity within xenoliths is coplanar with the main foliation of the TKts in structurally lower positions. In addition, fabric intensity in host TKts increases along the margins of xenoliths.

TKts Petrology and Geochemistry

Unit TKts is a compositionally heterogeneous intrusive unit with numerous internal contacts consistent with a composite origin. Modal abundances of constituent minerals vary but include hornblende, biotite, K-feldspar, and quartz. Composition ranges from diorite to true granite, with hornblende nearly absent in the latter. In general, unit TKts is predominately granodioritic with coarse hornblende and biotite, and accessory titanite, zircon, and apatite. Both magnetite and ilmenite have been identified as opaque phases. Medium- to coarse-grained, unit TKts is predominately equigranular, with local porphyritic and porphyroclastic varieties occurring wherein K-feldspar is slightly larger (~1.5 cm) than the quartzofeldspathic groundmass (~0.5 cm average grain size; Truskowski and others, 2024b).

Twelve whole-rock major- and trace-element analyses were performed on unit TKts, and two additional analyses were performed on the younger Tbqm unit (Truskowski and others, 2024a). For all samples, SiO_2 ranges from 55 to 70 weight percent, and the sum of total alkalis ($Na_2O + K_2O$) is 5.0–6.5 weight percent. Using the classification scheme of Frost and Frost (2008), samples are magnesian and calcic to calc-alkalic. Normalized to chondrites (Sun and McDonough, 1989), samples from both units display systematic depletion in high field strength elements with corresponding large ion lithophile enrichments and are light-rare-earth-element (LREE)-enriched, with sloping LREE–middle rare earth elements (MREE) and flat heavy rare earth elements (HREE) trends (fig. 6). They do not exhibit a strong negative Eu anomaly and have Eu/Eu* values ranging from 0.8 to 1.2, indicating minimal plagioclase fractionation. Compositionally, unit TKts samples are indistinguishable from unit Tbqm. These results indicate the units share all the hallmarks of generation within a suprasubduction zone setting and likely formed as a part of a continental arc magmatic event during active subduction.

TKts Deformational History

Intrusive rocks belonging to TKts are variably deformed, and nearly all host-rock screens in unit MzPzgm are pervasively deformed. All fabrics are granoblastic, indicating that elevated temperature outlasted deformation. The main structural fabrics of strong gneissosity/foliation are defined by compositional banding in xenolithic paragneiss rocks and flattened feldspar and biotite, as well as fractured and aligned hornblende, in meta-intrusive rocks. This main foliation becomes increasingly intense toward the west, structurally downward within the TKts unit. Mineral stretching lineations plunge moderately to the east and preserve asymmetries locally, consistent with west-vergent, reverse-sense motion during deformation (Fig. 5C). These features are consistent with current definitions of the Coast shear zone (Gehrels and others, 2009), a 68–56 Ma east-side-up contractional shear zone near the tonalite sill (unit TKts in the map area). Two existing U-Pb zircon ages from Gehrels (2000) indicates crystallization of TKts from 68–63 Ma. These constraints indicate that emplacement corresponded to contractional deformation focused along the western margin of the tonalite sill further to the south (Regan et al., 2024).

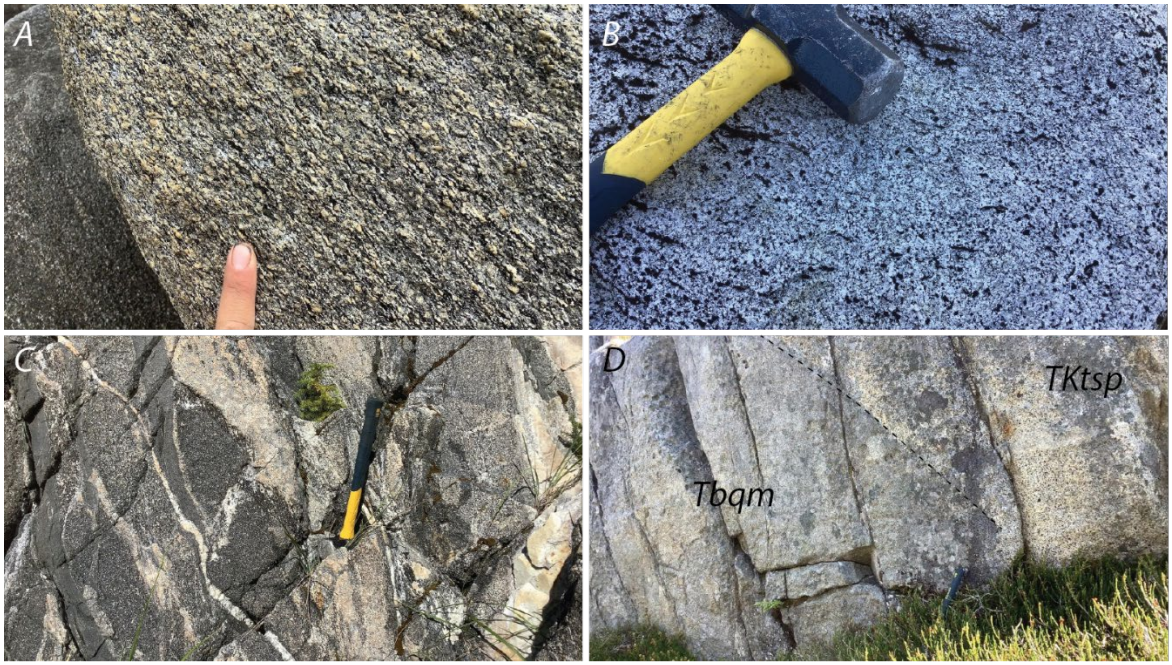

Figure 5. Field photographs from units TKts and Tbqm. **A.** Strongly foliated hornblende granodiorite near the structural base of TKts. **B.** Relatively undeformed TKts near the structural top of the unit. **C.** Strongly deformed, boudinaged, and disrupted amphibolite xenoliths of MzPzgm within the upper half of unit TKts (note: boudinage rotation indicates reverse-sense, top-to-the-west relative motion). **D.** Steeply dipping contact between units TKts and Tbqm.

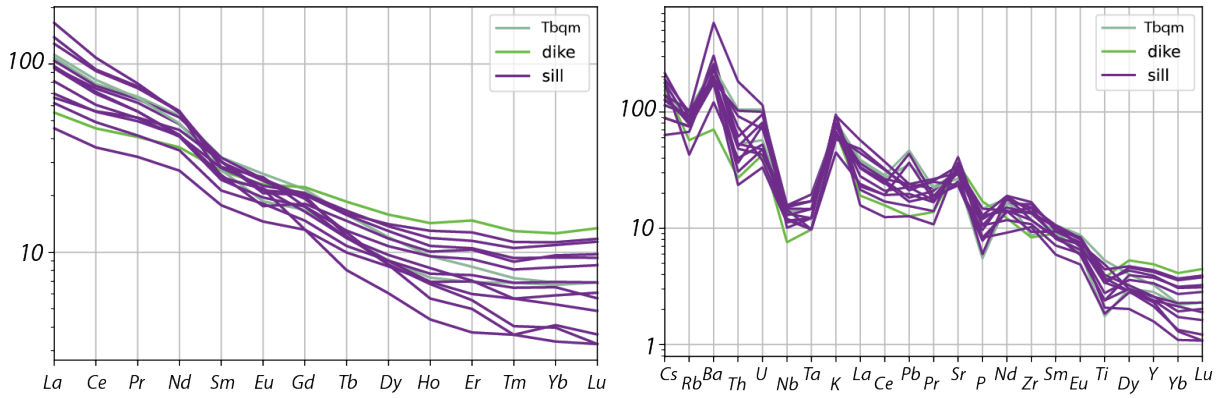

Figure 6. Spider diagrams normalized to primitive mantle after Sun and McDonough (1989) for units TKts and Tbqm, and a TKts mafic dike cross-cutting these lithologies. **A.** REE diagram displaying steep LREE slope and relatively flat HREE slope with no Eu anomaly. **B.** Incompatible element diagram showing systematic depletions in high field strength elements (HFSE) and enrichments in large ion lithophile elements (LILE) consistent with a suprasubduction zone origin.

STUDY 4: MOUNT KASHAGNAK PLUTON

The Mount Kashagnak region is located within the Chilkat block northwest of the City of Haines (fig. 2) and is underlain by a large intrusive complex (Mount Kashagnak pluton). Redman (1984) mapped three individual units defining a concentrically zoned pluton that ranges from: (1) an outer hornblende diorite (Kkhd), (2) a middle unit of porphyritic hornblende quartz monzonite to quartz diorite (Kkgd), to (3) a porphyritic quartz monzonite core (Kqm). The Mount Kashagnak pluton encompasses numerous Alaska Resource Database File localities, mostly associated with gold (Au), silver (Ag), and copper (Cu) mineralization along the margins of the system (Redman, 1984). A single multi-grain zircon U-Pb analysis of the intrusion sampled from a fault-bound fragment of Kkgd adjacent to Lutak Road yielded a crystallization age of 83 ± 2 Ma (Gehrels, 2000). We conducted a ground traverse and helicopter-supported regional sampling of the pluton to evaluate the continuity of zonation, provide modern analytical context for the intrusive system, and determine the relationship of the intrusive system to critical metal mineralization in the Haines area.

The Mount Kashagnak pluton is a canoe-shaped intrusion approximately 30 km long, with its long axis oriented southeast–northwest. Foliations defined by the alignment of minerals are common and well-developed in the structurally lower portions of the pluton. The northeastern margin of the pluton is truncated by the Chilkoot fault segment. Ten samples were analyzed for 72 elements, and geochemical analyses were performed throughout the pluton in addition to standard petrographic analysis for each unit (Truskowski and others, 2024a; fig. 7).

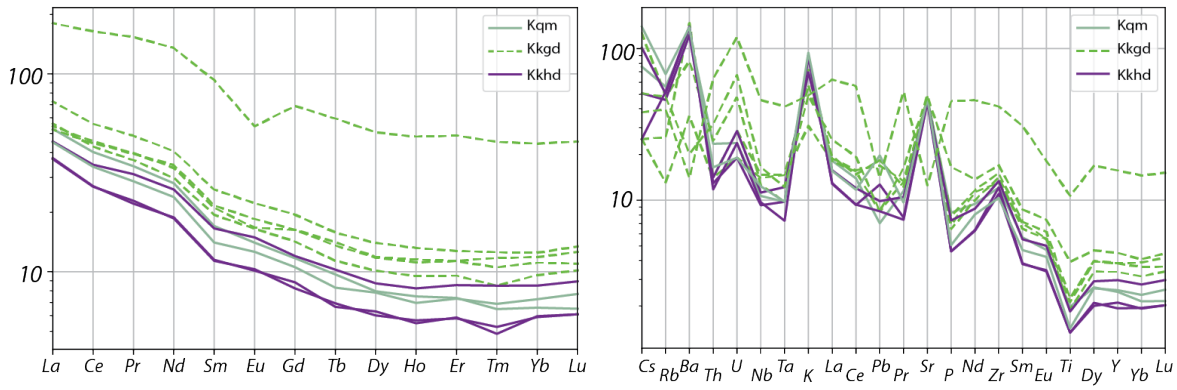

Figure 7. Spider diagrams normalized to primitive mantle after Sun and McDonough (1989) from the Mount Kashagnak pluton. **A.** REE diagram displaying steep LREE slope and relatively flat HREE slope with no europium (Eu) anomaly. **B.** Incompatible element diagram showing systematic depletions in HFSE and enrichments in LILE consistent with a suprasubduction zone origin; note strong potassium (K) and strontium (Sr) enrichment.

These new geochemical results corroborate interpretations of Redman and others (1984). The outer hornblende diorite (unit Kkhd) ranges from 58.06 to 63.53 weight percent SiO_2. Lenses of more mafic, meter-scale, true gabbro are present only within this unit. Unit Kkhd contains abundant hornblende and biotite, as well as large K-spar megacrysts absent from the adjacent, middle unit Kkgd. Kkgd is predominately equigranular hornblende granodiorite with sparse K-spar megacrysts that increase in abundance toward the inner Kqm unit. The innermost and structurally highest unit (Kqm) is a quartz monzonite with abundant K-spar megacrysts that exceed 15 mm in length in a fine-grained, equigranular matrix of quartz,

plagioclase, K-spar, and biotite. Megacrystic K-spar increases in abundance structurally upward, consistent with a late orthomagmatic origin, which may have also catalyzed mineralization surrounding the intrusion.

STUDY 5: ROCK MASS CLASSIFICATION

To characterize rock mass, both the intact rock strength and the discontinuities within the rock mass must be considered. Rock masses typically have several types of discontinuities present, such as fractures, joints, faults, foliations, bedding planes, and bedrock contacts. In certain orientations, these discontinuities allow blocks to be released from the intact mass, generating a rockslide or rockfall. We collected data at five stations, 23MCL009, 23MCL010, 23MCL011, 23MCL012, and 23MCL023 (Truskowski and others, 2024b; fig. 8), for rock mass classification and kinematic analysis.

This investigation used the Rock Mass Rating (RMR) system developed by Z. T. Bieniawski (1989) to evaluate rock strength and quality; all procedures, definitions, tables, and correlation charts used in this study are found in chapter four of Engineering Rock Mass Classifications by Bieniawski (1989). The RMR relies on six parameters to classify the rock mass: (1) intact rock strength, (2) rock quality designation (RQD), (3) spacing of the discontinuities, (4) condition of the discontinuities, (5) groundwater conditions, and (6) a rating adjustment based on the strike and dip orientations of the discontinuities as they compare to the slope. This adjustment considers the parallelism of the discontinuity to the slope face (i.e. strike), and its steepness (i.e. dip). Discontinuities that dip into the rock mass or are very shallow are less likely to slide and therefore have a “favorable” orientation. Those that dip out of the slope and have steeper dip angles are more likely to slide and have an “unfavorable” orientation. For site locations where intact rock strength laboratory testing was not conducted, rock strength values were determined using the field identification methods described by the International Society of Rock Mechanics (Ulusay and Hudson, 2007). Because no drilling was conducted as part of this project, RQD values were estimated (Bieniawski, 1989, chart D).

Using the structural mapping data described above, we then used RocScience Dips software for kinematic analysis. This software projects joint orientations onto equal-area, equatorial stereonets to determine if they have the potential to cause wedge sliding, planar sliding, or toppling failures.

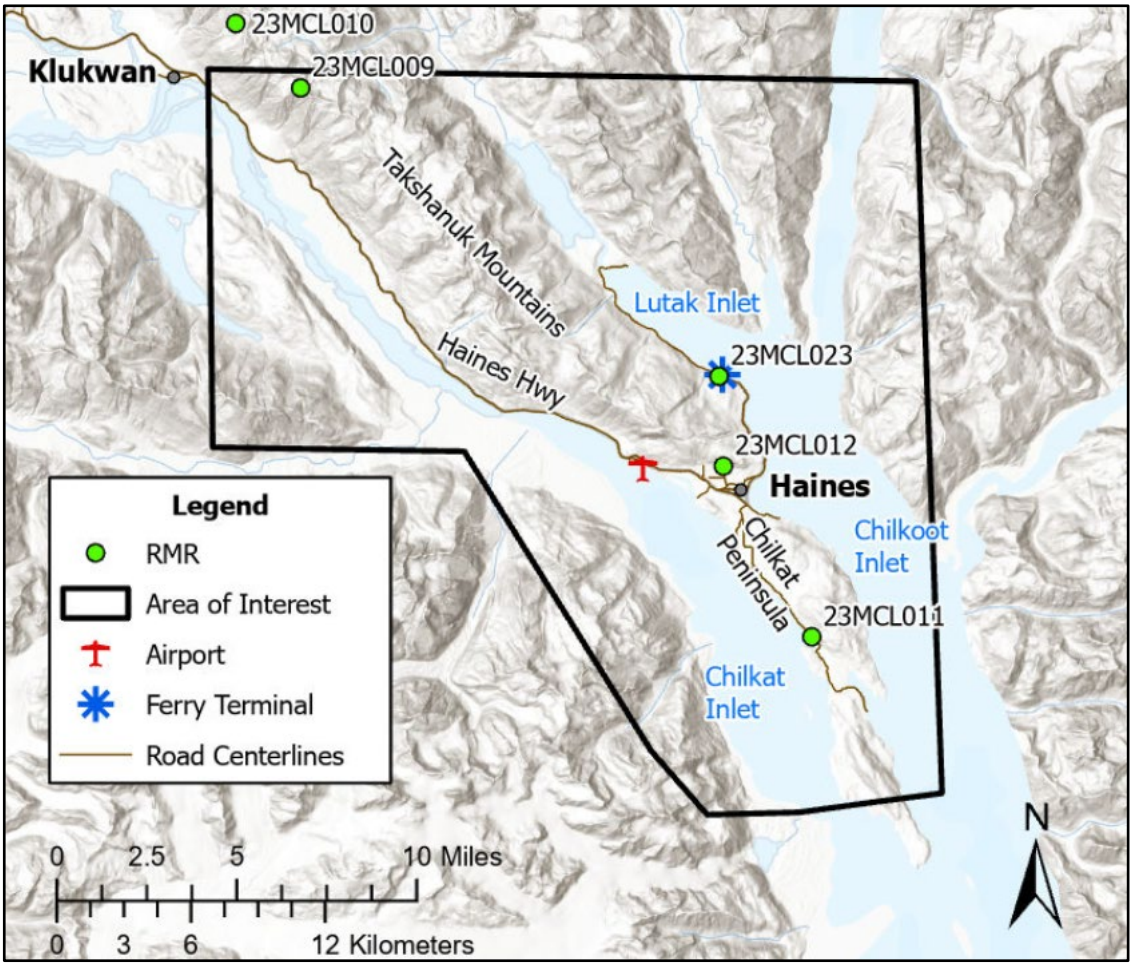

Figure 8. Map showing the Rock Mass Rating (RMR) locations.

RMR Calculations

A summary of RMR classification parameters and ratings for each of the five evaluated stations is provided in table 2, and the final ratings, class numbers, and associated cohesion and friction angles are provided in table 3. Cohesion and friction angles can be used for further analysis in factor of safety calculations for a rock block.

Station 23MCL009 is located at the top of the Haines Highway Milepost 19 debris flow catchment (fig. 8). The bedrock is very strong, slightly weathered to weathered granodiorite. The rock mass is controlled by moderately spaced, low-to medium-persistence joints that have open apertures. The joints are unfilled and have rough, slightly weathered to unweathered surfaces. Potential and observed rockfall blocks are cubic-shaped and range from 0.25 to 0.50 m across their largest dimensions. Based on the strike-dip orientation of the joints to the rock face, an adjustment of "fair" was applied using the Discontinuity Adjustment for Slopes, which was set at -25 (table 2). The final adjusted RMR rating is 59, which correlates to "fair rock" (table 3).

Table 2. RMR classification parameters and their ratings (Bieniawski, 1989)

	23MCL009	23MCL010	23MCL011	23MCL012	23MCL023
Intact Rock Strength	12[I]	12[II]	12[III]	7[IV]	2[IV]
RQD (correlated, %)	17	17	17	17	3
Discontinuity Spacing	15	10	15	10	8
Discontinuity Condition	25	25	20	20	10
Groundwater	15	15	15	15	10
Discontinuity Adjustment for Slopes	-25	-25	-25	-25	-25

[I] Intact rock strength value comes from uniaxial compressive strength lab results from samples 23MCL001B and D (Nicolazzo and others, 2024b).

[II] Intact rock strength value comes from uniaxial compressive strength lab results from samples 23MCL002A, B, C, D, and F (Nicolazzo and others, 2024b).

[III] Intact rock strength value comes from uniaxial compressive strength lab results from samples 23MCL011 (Nicolazzo and others, 2024b).

[IV] No lab testing was conducted at this station. Rock material strength value was determined using the field identification (ISRM, 1977).

Table 3. RMR final ratings

	23MCL009	23MCL010	23MCL011	23MCL012	23MCL023
RMR Rating	59	54	54	44	8
Class No.	III	III	III	III	V
Description	Fair rock	Fair rock	Fair rock	Fair rock	Very poor rock
Friction Angle	35	35	35	35	15
Cohesion (kPa)	200-300	200-300	200-300	200-300	<100
Correlated RQD	75-90	75-90	75-90	75-90	<25

Station 23MCL010 is located at the top of the Haines Highway Milepost 23 debris flow catchment outside of the mapped area (fig. 8). The bedrock is very strong, slightly weathered magnetite gneiss. The rock mass is controlled by moderate-to-close-spaced, low-to-medium-persistence joints that have moderately to open apertures. The joints are unfilled and have rough to smooth, slightly weathered to unweathered surfaces. Potential and observed rockfall blocks are cubic-shaped and range from 0.25 to 1.0 m across their largest dimensions. Based on the strike-dip orientation of the joint, an adjustment of "fair" was applied (table 2). The final adjusted RMR rating is 54, which correlated to "fair rock" (table 3).

Station 23MCL011 is located south of Haines off Mud Bay Road (fig. 8). The bedrock is medium weak, slightly weathered to weathered metavolcanics. The rock mass is controlled by moderately spaced, low-to-medium-persistent joints that have tight to moderately open

apertures. The joints are unfilled and have slightly rough to smooth, slightly weathered to moderately weathered surfaces. Potential and observed rockfall blocks are cubic in shape and range from 0.25 to 0.50 m across their largest dimensions. Based on the strike-dip orientation of the joints, an adjustment of "fair" was applied (table 2). The final adjusted RMR rating is 54, which correlates to "fair rock" (table 3).

Station 23MCL012 is located at the rock quarry just north of downtown Haines (fig. 8). The bedrock is strong, slightly weathered to weathered granodiorite. The rock mass is controlled by moderate-to-close-spaced, low-to-high-persistence joints that have moderately to open-apertures that are slightly rough to smooth, unfilled, and have slightly weathered surfaces. Potential and observed rockfall blocks are cubic in shape and range from 0.25 to 1.0 m across their largest dimensions. Based on the strike-dip orientation of the joint, an adjustment of "fair" was applied (table 2). The final adjusted RMR rating is 44, which correlates to "fair rock" (table 3).

Station 23MCL023 is located off Lutak Road, west of the road, across from the ferry terminal (fig. 8). The bedrock is medium-weak to weak, slightly weathered to moderately weathered phyllite. The rock mass is controlled by closely to very-closely spaced, low-to-very-low-persistence joints that have moderately open to tight apertures. The joints are damp with smooth to slickensided, moderately weathered to highly weathered surfaces. Potential and observed rockfall are platy in shape and range from 0.10 to 0.25 m across their largest dimensions. Based on the strike-dip orientation of the joint, an adjustment of "fair" was applied (table 2). The final adjusted RMR score is 8, which correlated to "very poor rock" (table 3).

Kinematic Analysis

Kinematic analysis was performed using RocScience Dips software to project joint orientation onto equal-area, equatorial stereonets. The analysis was used to determine if joint sets or combinations of joint sets within certain parameters have the geometric potential to generate rockfall as sliding or toppling failures (i.e. the joint intersections or poles fell within the critical areas for sliding or toppling failure); it does not predict future failure. Major joint sets are reported here, and the full failure potential plots for all five stations are presented in Appendix A.

The mapping exercise identified three major joint sets in the rock mass at station 23MCL009 that contribute to rock slope instability (table 4). These joint sets were projected onto a stereonet plot of pole vectors (fig. 9), which indicates possible wedge sliding and direct toppling failures at this location (fig. A1).

Table 4. Station 23MCL009 major joint set summary.

Joint Set ID	Average Dip (degrees)	Average Dip Direction (Azimuth)	Average Strike (Azimuth)
Joint 1	83	240	150
Joint 2	78	149	59
Joint 3	35	266	269

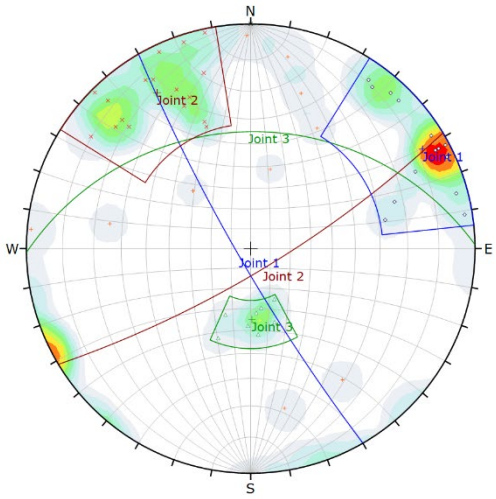

Figure 9. Station 23MCL009 major joint sets.

The mapping exercise identified three major joint sets in the rock mass at station 23MCL010 that contribute to rock slope instability (table 5). Joint sets were projected onto a stereonet plot of pole vectors (fig. 10), which indicates possible planar sliding, wedge sliding, flexural toppling, and direct toppling failures (fig. A2).

Table 5. Station 23MCL010 major joint set summary.

Joint Set ID	Average Dip	Average Dip Direction (Azimuth)	Average Strike (Azimuth)
Joint 1	67	239	149
Joint 2	59	139	49
Joint 3	55	50	321

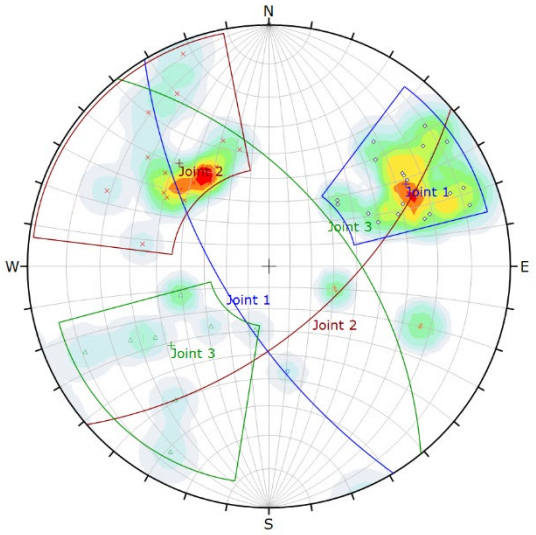

Figure 10. Station 23MCL010 major joint sets.

The mapping exercise identified three major joint sets in the rock mass at station 23MCL011 that contribute to rock slope instability (table 6). Joint sets were projected onto a stereonet plot of pole vectors (fig. 11), which indicates possible planar sliding, wedge sliding, flexural toppling, and direct toppling failures (fig. A3).

Table 6. Station 23MCL011 major joint set summary.

Joint Set ID	Average Dip	Average Dip Direction (Azimuth)	Average Strike (Azimuth)
Joint 1	74	226	161
Joint 2	77	177	88
Joint 3	55	38	309

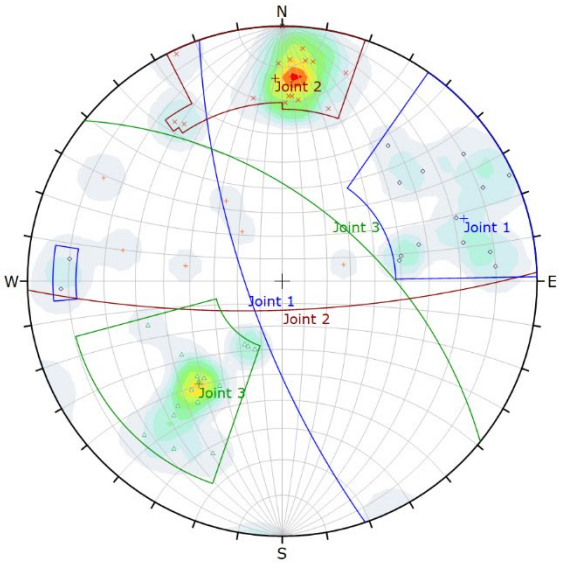

Figure 11. Station 23MCL011 major joint sets.

The mapping exercise identified four major joint sets in the at station 23MCL012 rock mass contributing to rock slope instability (table 7). Joint sets were projected onto a stereonet plot of pole vectors (fig. 12), which indicates possible planar sliding, wedge sliding, flexural toppling, and direct toppling failures (fig. A4).

Table 7. Station 23MCL012 major joint set summary.

Joint Set ID	Average Dip	Average Dip Direction (Azimuth)	Average Strike (Azimuth)
Joint 1	47	262	178
Joint 2	80	164	85
Joint 3	64	79	349
Joint 4	57	222	260

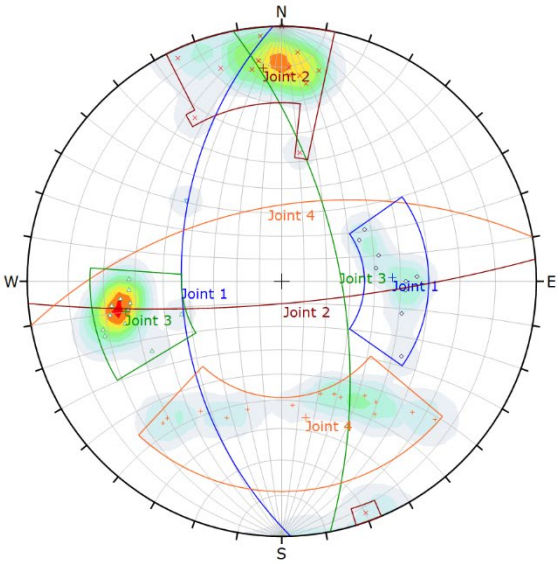

Figure 12. Station 23MCL012 major joint sets.

The mapping exercise identified four major joint sets in the rock mass at station 23MCL023 contributing to rock slope instability (table 8). Joint sets were projected onto a stereonet plot of pole vectors (fig. 13), which indicates possible wedge sliding, flexural toppling, and direct toppling failures (fig. A5).

Table 8. Station 23MCL023 major joint set summary.

Joint Set ID	Average Dip	Average Dip Direction (Azimuth)	Average Strike (Azimuth)
Joint 1	82	250	180
Joint 2	84	53	324
Joint 3	47	338	246
Joint 4	11	136	46

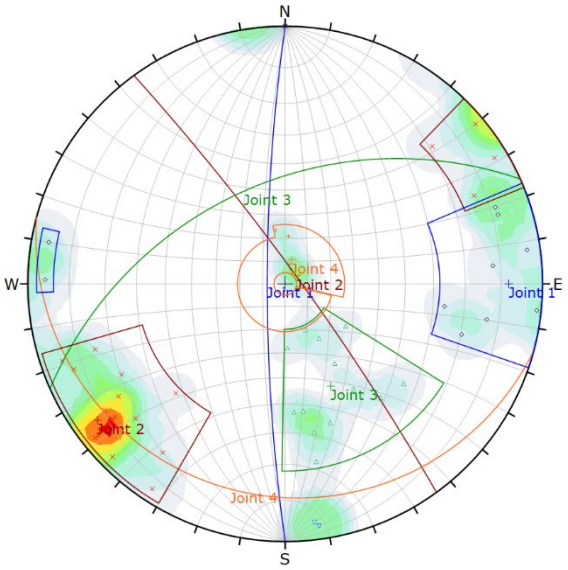

Figure 13. Station 23MCL023 major joint sets.

MAP UNITS

SURFICIAL UNIT DESCRIPTIONS

ALLUVIAL DEPOSITS

Qa ALLUVIUM, UNDIFFERENTIATED (Holocene)—Moderately to well-sorted gravel, sand, and silt encompassing channel and overbank deposits of small streams.

Qaa ACTIVE FLOODPLAIN ALLUVIUM (Holocene)—Moderately to well-sorted gravel and sand with minor silt, deposited as river bars and at the mouth of rivers. Experiences inundation by modern streams every five years or less (Chapin and others, 2006, as cited in Reger and others, 2012).

Qai INACTIVE FLOODPLAIN ALLUVIUM (Holocene–Upper Pleistocene)—Moderately to well-sorted, very fine- to fine-grained sand, and silt deposited by modern rivers as overbank deposits, overlying gravelly and sandy bedload deposits. Encompasses all deposits from modern rivers subject to inundation in greater than 5-year intervals, including stream-terrace alluvium and abandoned floodplain alluvium (comparative unit from Reger and others, 2012).

Qaf ALLUVIAL FAN (Holocene–Upper Pleistocene)—Moderately stratified, poorly sorted gravel and cobbles with a sandy matrix. Deposited subaerially by streams where their gradient is rapidly reduced, often as they emerge from the mountain front. Alluvial processes are dominant. Variable thickness of 10 meters or more. Active alluvial fans along Lutak Road and Haines Highway may present a risk to local infrastructure.

Qad DELTA DEPOSITS (Holocene–Upper Pleistocene)—Moderately well-sorted, subrounded sand and silt with lesser gravel. Deposited as prograding delta aprons of the Ferebee River and Katzehin River drainages.

COLLUVIAL DEPOSITS

Qc COLLUVIUM (Holocene)—Silty gravel and cobbles to sand and silt, with organic material that has moved downslope under the influence of gravity. Composition, grain-size distribution, and organic content are variable. Steep, glacially smoothed bedrock slopes are especially susceptible to slow-moving, downslope creep, resulting in the mixing of till, elevated beach, and elevated marine deposits. Material may move rapidly during periods of heavy rainfall, resulting in a mix of snow and avalanche debris with talus deposits. May include landslide and talus deposits too small to differentiate at the scale of mapping.

Qca MIXED COLLUVIUM and ALLUVIUM (Holocene–Upper Pleistocene)—Massive to poorly stratified inorganic silt mixed with sandy, angular to subangular gravel. Colluvial processes are dominant over alluvial. May be fan-shaped where deposited by debris flows at the mouth of narrow valleys or elongated in cirques and glacially steepened valleys. Locally includes glacial drift modified by colluvial and alluvial processes, as well as debris flow deposits too small to differentiate at the scale of mapping.

Qct TALUS (Holocene)—Angular cobble- to boulder-sized rock rubble and minor sand. Found along mountain fronts where debris has fallen from near-vertical bedrock cliffs. Loosely packed, high void ratio, and prone to reactivation.

Qcl LANDSLIDE (Holocene–Upper Pleistocene)—Mixture of large bedrock blocks; angular, subangular, rounded, and subrounded gravel, cobbles, and boulders; and sand and silt, deposited on steep slopes or drainages by creeping, flowing, and sliding of failed bedrock or unconsolidated surficial deposits. Includes debris flows large enough to differentiate at the scale of mapping.

MARINE DEPOSITS

Qmey YOUNGER EMERGENT MARINE DEPOSITS (Holocene)—Clay and silt with minor sand interbedded with coarser deltaic deposits and alluvium in the upper parts. Elevated due to isostatic uplift during regional deglaciation and/or tectonic processes (modified from March, 1987).

Qme OLDER EMERGENT MARINE DEPOSITS (Upper Pleistocene)— Predominantly silt and clay, with some sand, medium gray color. Organic-rich zones up to one meter thick are found locally. May contain marine fossils. Deposited in fjords as fine-grained material from glaciers, rivers, and streams and subsequently uplifted by isostatic rebound and/or tectonic processes (Lemke and Yehle, 1972; March, 1987).

BEACH DEPOSITS

Qb MODERN BEACH DEPOSITS (Holocene)—Chiefly loose, moderately well-sorted, stratified, fine- to coarse-grained sand, subrounded gravel, and angular to subangular boulders. Deposits extend from mean low water to the upper limits of wave action (modified from March, 1987).

Qeb ELEVATED BEACH DEPOSITS (Holocene–Upper Pleistocene)—Moderately well-sorted, stratified deposits of elevated shore and delta sediments composed of rounded to subrounded sand and gravel. Elevated above sea level by isostatic rebound and/or tectonic processes (modified from March, 1987). Reaches an elevation of approximately 90 m, maybe as high as 180 m.

GLACIAL DEPOSITS

Qgo GLACIAL OUTWASH (Holocene–Upper Pleistocene)—Poorly to moderately well-sorted, stratified, subrounded gravel and sand with lesser silt and cobbles deposited by glacial meltwater. Includes meltwater deposits of modern glaciers and Pleistocene outwash terraces on modern stream margins and inlets. May be widespread beneath elevated marine deposits (Lemke and Yehle, 1972).

Qgf GLACIAL OUTWASH FAN (Holocene)—Poorly sorted, stratified gravel and sand deposited by glacial meltwater near the termini of glaciers. Unit description after March (1987).

Qgr ROCK GLACIER (Holocene–Upper Pleistocene)—Heterogeneous deposits of angular to subangular gravel, cobbles and boulders with an ice matrix.

Characterized by hummocky or lobate (stair-step) landscape, occurring chiefly in cirques. Subject to slow downslope movement where active.

Qgt GLACIAL TILL (Holocene–Upper Pleistocene)—Light to medium gray to greenish gray, poorly sorted gravel, sand, and silt, with lesser clay and cobbles. Gravel and cobbles are subrounded to subangular and are chiefly clasts of local bedrock. Upper 50 centimeters to one meter may be oxidized yellowish orange to orangish brown. Deposited directly by glacial ice and may include ground moraine, end moraine, and areas of thinly covered bedrock. Minor ice-cored deposits may be present in recently deglaciated areas. Locally modified by colluvial and/or fluvial processes.

Qgl GLACIAL LACUSTRINE (Upper Pleistocene)—Well-sorted deposit of predominantly clay and silt deposited by a proglacial lake impounded behind a moraine that separates Chilkoot Lake from Lutak Inlet in the north-central part of the map area.

PALUDAL DEPOSITS

Qp PALUDAL (Holocene)—Very dark brown organic, fibrous, and locally woody, peat; interlayered with thin beds of organic silt and sand. Thickness variable.

MANMADE DEPOSITS

Qhf ARTIFICIAL FILL (Holocene)—Areas of human-emplaced fill. Also found in road embankments and building site fill, but these are too small to differentiate at this map scale.

BEDROCK UNIT DESCRIPTIONS

"TAKHIN BLOCK"

Igneous Rocks

Tgd GRANODIORITE (Tertiary)—Medium-grained, equigranular, hornblende–biotite granodiorite and hornblende–biotite quartz diorite. Description from Gilbert and others (1987).

Tcd CATACLASTIC DIORITE (Tertiary)—Fine- to medium-grained hornblende diorite or granodiorite that exhibits strong cataclastic foliation. Description from Gilbert and others (1987).

Tdf FOLIATED DIORITE (Tertiary)—Medium-grained, equigranular quartz diorite and hornblende diorite that generally display both flow foliation and compositional layering. Description from Gilbert and others (1987).

Keg GRANODIORITE AND OTHER PLUTONIC ROCKS (Cretaceous)—Medium- to coarse-grained, equigranular hornblende–biotite granodiorite and diorite Minor quartz diorite and tonalite. Generally massive but locally foliated (Gilbert, 1988). Inferred to be in igneous contact with Pzvs to the east.

Kgdf FOLIATED GRANODIORITE (Cretaceous)—Light gray, very fine- to coarse-grained, weakly to moderately foliated biotite–hornblende granodiorite. Metasedimentary and igneous xenoliths locally common. Locally porphyritic, with biotite and

hornblende phenocrysts 1- to 10-cm long. In igneous contact with Pzvs to the east.

Metasedimentary Rocks

MDph BLACK PHYLLITE (Mississippian–Devonian)—Locally tightly folded black phyllite, black slate, and dark gray metasiltstone. Locally limonitic and commonly contains up to 25 percent phyllitic calc-siltstone and 25 percent thin-bedded, fissile, sooty limestone. Description from Gilbert and others (1987).

MDl SOOTY LIMESTONE (Mississippian–Devonian)—Sheared, laminated, gray, sooty limestone with thin bioclastic beds. Age is likely Devonian or Mississippian, based on preliminary identification of conodonts from a single locality in the unit. Description from Gilbert and others (1987).

Four-Winds Complex

Pzv METAVOLCANIC ROCKS (Ordovician–Silurian)—Green-gray, fine-grained actinolite schist; quartz schist; calc-schist and carbonaceous phyllite; and minor slate. Intercalated marble bodies up to 100 m thick locally. Mylonitic to ultra-mylonitic at the contact with Pzam to the west. To the north, this unit can also include mafic and felsic schist, black phyllite, and calc-schist that represent metamorphosed basalt, intermediate and silicic flows and pyroclastic rocks, volcanogenic sediments, impure chert, shale, and calc-siltstone (Gilbert and others, 1987).

Pzvs METAVOLCANIC AND METASEDIMENTARY ROCKS (Silurian)—Variable assemblage of schistose volcanoclastic rock, dark gray slate, metabasite, and marble. Locally includes minor amounts of gneiss, felsic schist, or chert. May be hornfelsed near contact with Keg to the west. Description from Gilbert (1988).

Pzam CALC-SCHIST (Silurian)—Light gray to light-tannish brown to blue-green calc-schist, minor hornblende–biotite schist, quartzite, and siliceous marble. May be finely intercalated at meter scale.

CHILKAT BLOCK

Plutonic and Volcanic Rocks

Tlqm LEUCOCRATIC QUARTZ MONZONITE (Tertiary)—Occurs as small plugs and dikes concentrated in the Chilkat block, south and west of Tukgaho Peak. Plugs are medium-grained granular rocks, with 40 percent K-feldspar, 40 percent plagioclase, 20 percent quartz, and 1–3 percent biotite. Dikes have a sucrosic texture and may contain small red garnets. This rock intrudes the metabasalt (Trmb) and Mount Kashagnak pluton (Kqm/Kkgd) (Redman and others, 1984).

Kkhd HORNBLENDE DIORITE (Cretaceous)—Medium- to coarse-grained hornblende diorite to quartz diorite. Moderately foliated, seriate rock composed of plagioclase feldspar and hornblende with minor quartz, K-feldspar, and trace magnetite. Epidote commonly replaces hornblende. Rare K-feldspar megacrysts near the upper contact

with middle Mount Kashagnak intrusive unit. Grain size ranges from 2 to 6 mm and exhibits a seriate texture. Hornblende is lineated. Local meter-scale layers of hornblende gabbro occur with similar textures to main hornblende diorite phase. Fresh surfaces are generally dark gray to green; weathers dark brown. Unit comprises the outer zone of the Mount Kashagnak plutonic complex.

Kkgd GRANODIORITE (Cretaceous)—Leucocratic, medium-grained, porphyritic, foliated hornblende granodiorite and minor quartz monzodiorite and quartz monzodiorite. Mineralogy consists of 30–40 percent plagioclase, 20–30 percent K-feldspar, 5–15 percent quartz, 5–20 percent hornblende, and accessory magnetite. Petrographically identified late epidote is common, particularly around primary hornblende. Coarse, pink K-feldspar megacrysts occur throughout the unit and range in size from 1–6 cm. Fresh surfaces are generally pale gray to pink, with buff to light gray weathering. Intermediate unit of the Mount Kashagnak plutonic complex between the rim and core.

Kqm QUARTZ MONZONITE (Cretaceous)—Leucocratic, medium-grained, hornblende–biotite quartz monzonite porphyry with distinctive K-feldspar megacrysts up to 7 cm in length. K-feldspar megacrysts contain biotite inclusions whose cleavage parallels host crystal faces. Matrix is equigranular with grain sizes ranging from 2–4 mm. Biotite ranges from 10–15 percent with hornblende comprising approximately 5 percent. Quartz ranges from 10–15 percent with minor matrix K-feldspar (~10 percent). Including megacrysts, K-feldspar accounts for up to 20–30 percent of the rock. Titanite and magnetite are common accessory minerals. Core of the Mount Kashagnak plutonic complex.

Kum HORNBLENDE PYROXENITE (Cretaceous)—Coarse- to very coarse-grained hornblende pyroxenite. Subhedral crystals of hornblende, pyroxene, and plagioclase 0.5–3 cm long. Majority of rock (80 percent) is composed of hornblende pseudomorphs after pyroxene. Hornblende–plagioclase–thulite pegmatites are abundant and display sharp and gradational contacts with the pyroxenite. Locally, pegmatites occur within fine-grained biotite–hornblende pyroxenite. Unit is intruded by KKhd and contains abundant inclusions of Kp (Redman and others, 1984).

Kp PYROXENITE AND HORNBLENDITE (Cretaceous)—Fine- to very coarse-grained clinopyroxenite and hornblendite with up to 5 percent biotite, and variable magnetite. Crosscut by intrusions of the same mineralogy and numerous generations of mono-mineralic veins of hornblende, clinopyroxene, and magnetite. Malachite staining is common. K-Ar hornblende analysis yielded 99 Ma and 96 Ma ages (MacKevett and others, 1974). Occurs as extremely abundant inclusions in unit Kum. Main ultramafic body is intensely fractured and contains veins of clinozoisite and dikes of quartz monzonite. Unit description from Gilbert and others (1987).

Trmb METABASALT AND METAVOLCANICS (Triassic)—Dark- to medium-green, dense to vesicular or amygdaloidal, aphanitic to finely and sparsely porphyritic, non- to

moderately foliated basalt. Pillows and columns are locally present. Commonly flow-banded. Tuffaceous layers are present south of Haines and outside of the map area. Two to 3 percent phenocrysts of hornblende and plagioclase <2mm in length, occasionally up to 1 cm. Rock is commonly altered to chlorite and epidote. Foliated and non-foliated volcaniclastic siltstone interbeds occur locally between lava flow deposits. Marginal autoclastic breccias occur locally. Gilbert and others (1987) cite associated Triassic fossils. Metabasalt is intruded by KKhd.

Sedimentary Rocks

Tk KOOTZNAHOO FORMATION (Tertiary)—Restricted to Kochu Island west of the Chilkat Peninsula. Light to medium gray, cobble-to-boulder clast- and matrix-supported conglomerate and lesser sandstone that form tabular packages several meters to 10s of meters thick. Internally disorganized. Clast compositions are dominated by subrounded to angular diorite cobbles to boulders up to 2 m long and subrounded to subangular metabasalt cobbles. A few foliated gneissic clasts are also present. Locally, monomictic beds of diorite boulders are matrix-supported. Rare, recessive intervals two to several meters thick and one notable covered interval of several tens of meters. One thin example of fissile black shale within a recessive interval. Entire succession greater than 100 m thick.

KJgn GRAVINA (Cretaceous–Jurassic)—Dark gray to black, very fine-grained sandstone, siltstone, and argillite. Platy to blocky weathering of tabular beds 1–150 cm thick. Plane-parallel laminated to locally crossbedded. Ripple marks and convolute bedding locally present. Larger weathering blocks are commonly carbonaceous, and the occurrence of red to green chert is locally common. Beds may be strongly folded at meter to decimeter scale and display well-defined cleavage parallel to fold axes. Unit is in fault contact with Trmb to the east.

CHILKOOT AND FEREBEE BLOCKS

Plutonic Rocks

Tbqm BIOTITE QUARTZ MONZONITE (Tertiary)—Fine- to medium-grained, locally porphyritic, biotite quartz monzonite to granite. Phenocrysts are coarse poikilitic plagioclase feldspar. Cross cuts MzPzgm and local TKts. Fresh surfaces are dark gray to pink, weathers dark gray. Color Index is <15.

TKts TONALITE SILL (Tertiary, Paleocene, and late Cretaceous)—Variably foliated and lineated, medium- to coarse-grained, hornblende- and biotite-bearing tonalite to granodiorite and minor quartz diorite. Exhibits a pervasive granoblastic texture. Deformed by a strong penetrative foliation and pervasive mineral lineation along the western edge of the unit, which dissipates to the east and structurally upward into a seriate and locally porphyritic texture, with plagioclase phenocrysts up to 2 cm. Accessory titanite is evident in outcrop locally. Fresh surfaces are light gray to

pink with dark gray weathering. Color Index varies from 5 to 40. Hosts numerous map-scale and smaller screens of MzPzgm.

Metamorphic Rocks

MzPzgm GNEISS AND MIGMATITE (Mesozoic and Paleozoic)—Biotite-bearing quartzofeldspathic paragneiss, foliated amphibolite, calc-silicate gneiss, migmatite, and minor orthogneiss forming screens ranging in size from meters to km-scale hosted in locally deformed unit TKts. Gneisses are granoblastic and contain a wide range in modal mineralogy, averaging approximately 45 percent quartz, 35 percent feldspar, 15 percent biotite, and minor hornblende. Gneissic layering in migmatitic paragneiss is defined by alternating bands of biotite-rich layers divided by variably thick granitic leucosome.

ACKNOWLEDGMENTS

This project was funded by the U.S. Geological Survey (USGS) National Cooperative Geologic Mapping Program under STATEMAP award number G22AC00606-00, 2022, and the State of Alaska General Fund. The views and conclusions contained in this document are those of the authors and should not be interpreted as necessarily representing the official policies, either expressed or implied, of the U.S. Government. Mention of trade names or commercial products does not constitute their endorsement by the USGS or by any branch or employee of the State of Alaska.

The authors would like to extend their gratitude to John Norton and Cindy Buxton for their generous hospitality, field advice, logistical support, and contributions to the project. Review comments by Trent Hubbard (DGGS) improved and clarified the content of this report.

REFERENCES

Allmendinger, R.W., Cardozo, Nestor, and Fisher, D.M., 2012, Structural geology algorithms: Vectors and tensors in structural geology: New York, Cambridge University Press, 289 p.

Angelier, J., and Mechler, P., 1977, Sur une methode graphique de recherche des contraintes principals egalment utilisable en tectonique et en seismologie: la methode des diedres droit: Bulletin de la Société Géologique de France, v. 19, p. 1,309–1,318.

Arthaud, Francois., 1969, Methode de determination graphique des directions de raccourcissement, d'allongement et intermediare d'une population de failles: Bulletin de la Société Géologique de France, v. 11, p. 729–737.

Bieniawski, Z.T., 1989, Engineering rock mass classifications, a complete manual for engineers and geologists in mining, civil and petroleum engineering: John Wiley & Sons, New York, 272 p.

Bingham, C.H., 1974, An antipodally symmetric distribution on the sphere, Annals of Statistics, v. 2, no. 6, p. 1,201–1,225. https://projecteuclid.org/download/pdf_1/euclid.aos/1176342874

Brothers, D.S., Elliott, J.L., Conrad, J.E., Haeussler, P.J., and Kluesner, J.W., 2018, Strain partitioning in Southeastern Alaska: Is the Chatham Strait fault active?: Earth and Planetary Science Letters, v. 481, p. 362–371. https://doi.org/10.1016/j.epsl.2017.10.017

Carrara, P.E., Ager, T.A., and Baichtal, J.F., 2007, Possible refugia in the Alexander Archipelago of southeastern Alaska during the late Wisconsin glaciation: Canadian Journal of Earth Science, v. 44, no. 2, p. 229–244. https://doi:10.1139/E06-081

Chardon, Dominique, Andronicos, C.L., and Hollister, L.S., 1999, Large-scale transpressive shear zone patterns and displacements within magmatic arcs: The Coast Plutonic Complex, British Columbia: Tectonics, v. 18, no. 2, p. 278–292.

Crawford, M.L., Hollister, L.S., and Woodsworth, G.J., 1987, Crustal deformation and regional metamorphism across a terrane boundary, Coast Plutonic Complex, British Columbia: Tectonics, v. 6, p. 343–361. https://doi.org/10.1029/TC006i003p00343

Darrow, M.M., Nelson, V.A., Grilliot, Michael, Wartman, Joseph, Jacobs, Aaron, Baichtal, J.F., and Buxton, Cindy, 2022, Geomorphology and initiation mechanisms of the 2020 Haines, Alaska landslide: Landslides, v. 19, p. 2,177–2,188. https://doi.org/10.1007/s10346-022-01899-3

Doubrovine, P.V., and Tarduno, J.A., 2008, A revised kinematic model for the relative motion between Pacific oceanic plates and North America since the Late Cretaceous: Journal of Geophysical Research: Solid Earth, v. 113, issue B12. https://doi.org/10.1029/2008JB005585

Evans, S.G., and Clague, J.J., 1999, Rock avalanches on glaciers in the Coast and St. Elias mountains, British Columbia: Proceedings, 13th Annual Vancouver Geotechnical Society Symposium, May 28, 1999, p. 115–123.

Ford, A.B., Palmer, C.A., Brew, D.A., Moore, T.E., and Dumoulin, J.A., 1996, Geochemistry of the andesitic Admiralty Island Volcanics; an Oligocene rift-related basalt to rhyolite volcanic suite of southeastern Alaska: U.S. Geological Survey Bulletin 2152, p. 177–204.

Frost, B.R., and Frost, C.D., 2008, A geochemical classification for feldspathic igneous rocks: Journal of Petrology, v. 49, p. 1,955–1,969.

Gehrels, G.E., 2000, Reconnaissance geology and U-Pb geochronology of the western flank of the Coast Mountains between Juneau and Skagway, southeastern Alaska, *in* Stowell, H.H.,

and McClelland, W.C., eds., Tectonics of the Coast Mountains, SE Alaska and Coastal British Columbia: Geological Society of America Special Paper 343, p. 213–234.

Gehrels, G.E., Rusmore, M., Woodsworth, G., Crawford, M., Andronicos, C., Hollister, L., Patchett, J., Ducea, M., Butler, R., Klepeis, K., Davidson, C., Friedman, R., Haggart, J., Mahoney, B., Crawford, W., Pearson, D., and Girardi, J., 2009, U-Th-Pb geochronology of the Coast Mountains batholith in north-coastal British Columbia: Constraints on age and tectonic evolution: Geological Society of America Bulletin, v. 121, p. 1,341–1,361.

Giesler, Dominique, Gehrels, G.E., Pecha, Mark, White, Chelsi, Yokelson, Intan, and McClelland, W.C., 2016, U-Pb and Hf isotopic analyses of detrital zircons from the Taku terrane, southeast Alaska: Canadian Journal of Earth Sciences, v. 53, p. 979–992. https://doi.org/10.1139/cjes-2015-0240

Gilbert, W.G., 1988, Preliminary geology of the northern Chilkat Range, southeastern Alaska: Alaska Division of Geological & Geophysical Surveys Report of Investigation 88-8, 2 sheets, scale 1:36,200. https://doi.org/10.14509/2456

Gilbert, W.G., Burns, L.E., Redman, E.C., and Forbes, R.B., 1987, Preliminary bedrock geology and geochemistry of the Skagway B-3 Quadrangle, Alaska: Alaska Division of Geological & Geophysical Surveys Report of Investigation 87-2, 2 sheets, scale 1:36,200. https://doi.org/10.14509/2426

Himmelberg, G.R., Brew, D.A., and Ford, A.B., 1991, Development of inverted metamorphic isograds in the western metamorphic belt, Juneau, Alaska: Journal of Metamorphic Geology, v. 9, p. 165–180.

Hudson, Travis, Plafker, George, and Dixon, Kirk, 1982, Horizontal offset history of the Chatham Strait fault, *in* Coonrad, W.L., ed., The United States Geological Survey in Alaska; accomplishments during 1980: U.S. Geological Survey Circular 844, p. 128–131.

Ingram, G.M., and Hutton, D.H.W., 1994, The Great Tonalite Sill: Emplacement into a contractional shear zone and implications for Late Cretaceous to early Eocene tectonics in southeastern Alaska and British Columbia: Geological Society of America Bulletin, v. 106, p. 715–728.

Kaufman, D.S., Young, N.E., Briner, J.P., and Manley, W.F., 2011, Alaska Palaeo-Glacier Atlas (Version 2), *in* Ehlers, J., and Gibbard, P.L., eds., Quaternary glaciations extent and chronology, part IV: A closer look: Developments in Quaternary Science, v. 15, p. 427–445. https://doi.org/10.1016/B978-0-444-53447-7.00033-7

Larsen, M.C., Bull, K.F., Truskowski, C.M., Walser, S.L., Regan, S.P., Gillis, R.J., Nicolazzo, J.A., and Darrow, M.M., 2025, Geologic map of the Haines-Takshunuk Mountains-Chilkat Peninsula area, Southeast Alaska, parts of the Skagway A-1, A-2, B-1, B-2, B-3 quadrangles, Alaska, *in* Larsen, M.C., ed., Geologic map and unit descriptions for Haines, Alaska: Alaska Division of Geological & Geophysical Surveys Preliminary Interpretive Report 2025-4A, 1 sheet, scale 1:50,000. https://doi.org/10.14509/31418

Lathram, E.H., 1964, Apparent right-lateral separation on Chatham Strait fault, southeastern Alaska: Geological Society of America Bulletin, v. 75, no. 3, p. 249–252. https://doi.org/10.1130/0016-7606(1964)75[249:ARSOCS]2.0.CO;2

Lemke, R.W., and Yehle, L.A., 1972, Reconnaissance engineering geology of the Haines area, Alaska, with emphasis on evaluation of earthquake and other geologic hazards: U.S. Geological Survey Open-File Report 72-229, 109 p., 2 sheets, scale 1:24,000.

Lesnek, A.J., Briner, J.P., Baichtal, J.F., and Lyles, A.S., 2020, New constraints on the last deglaciation of the Cordilleran Ice Sheet in coastal Southeast Alaska: Quaternary Research, v. 96, p. 140–160. https://doi.org/10.1017/qua.2020.32

Lesnek, A.J., Briner, J.P., Lindqvist, Charlotte, Baichtal, J.F., and Heaton, T.H., 2018, Deglaciation of the Pacific coastal corridor directly preceded the human colonization of the Americas: Science Advances, v. 4, no. 5. https://doi.org/10.1126/sciadv.aar5040

Loney, R.A., Brew, D.A., and Lanphere, M.A., 1967, Post-Paleozoic radiometric ages and their relevance to fault movements, northern southeastern Alaska: Geological Society of America Bulletin, v. 78, no. 4, p. 511–526.

MacKevett, E.M., Jr., Robertson, E.C., and Winkler, G.R., 1974, Geology of the Skagway B-3 and B-4 quadrangles, southeastern Alaska: U.S. Geological Survey Professional Paper 832, 33 p., 1 sheet, scale 1:63,360.

March, G.D., 1987, Surficial geology and materials-resources maps of the Skagway A-2 Quadrangle, Alaska: Alaska Division of Geological & Geophysical Surveys Report of Investigation 87-6, 2 sheets, scale 1:63,360. https://doi.org/10.14509/2429

Marrett, R.A., and Allmendinger, R.W., 1990, Kinematic analysis of fault-slip data: Journal of Structural Geology, v. 12, p. 973–986.

Motyka, R.J., Larsen, C.F., Freymueller, J.T., and Echelmeyer, K.A., 2007, Post Little Ice Age Glacial rebound in Glacier Bay National Park and surrounding areas: Alaska Park Science, v. 6, no. 1, p. 36–41.

Nicolazzo, J.A., Darrow, M.M., and Walser, S.L., 2024a, Soil index properties and radiocarbon ages of the Haines-Takshanuk Mountains-Chilkat Peninsula area STATEMAP project, Southeast Alaska: Alaska Division of Geological & Geophysical Surveys Raw Data File 2024-27. https://doi.org/10.14509/31415

Nicolazzo, J.A., Darrow, M.M., Larsen, M.C., and Walser, S.L., 2024b, Rock strength properties of the Haines-Takshanuk Mountains-Chilkat Peninsula area STATEMAP project, Southeast Alaska: Alaska Division of Geological & Geophysical Surveys Raw Data File 2024-28, 4 p. https://doi.org/10.14509/31416

Redman, E.C., 1984, An unconformity with associated conglomeratic sediments in the Berners Bay area of southeast Alaska, *in* Alaska Division of Geological & Geophysical Surveys, Short notes on Alaskan geology: Alaska Division of Geological & Geophysical Surveys Professional Report 86A, p. 1–4. https://doi.org/10.14509/2260

Redman, E.C., Retherford, R.M., and Hickok, B.D., 1984, Geology and geochemistry of the Skagway B-2 Quadrangle, southeastern Alaska: Alaska Division of Geological & Geophysical Surveys Report of Investigation 84-31, 34 p., 4 sheets, scale 1:40,000. https://doi.org/10.14509/2390

Regan, S.P., Holland, M.E., Waldien, T.S., Miller, M., Taylor, P., Kylander-Clark, A., Marble, S., and Hofmann, F., 2024, Orogen-scale inverted metamorphism during Cretaceous-Paleogene terminal suturing along the North American Cordillera, Alaska, USA: Geology, v. 52, no. 12, p. 933-938. https://doi.org/10.1130/G52614.1

Reger, R.D., Hubbard, T.D., and Gallagher, P.E., 2012, Surficial geology of Alaska Highway corridor, Tetlin Junction to Canada border, Alaska: Alaska Division of Geological & Geophysical Surveys Preliminary Interpretive Report 2012-1A, 25 p., 2 sheets, scale 1:63,360. https://doi.org/10.14509/23443

Sun, S., and McDonough, W.F., 1989, Chemical and isotopic systematics of oceanic basalts: Implications for mantle compositions and process, *in* Saunder, A.D., and Norry, M.J., eds., Magmatism in ocean basins: The Geological Society of London Special Publication, v. 42, p. 313–345.

Teyssier, Christian, Tikoff, Basil, and Markley, Michelle, 1995, Oblique plate motion and continental tectonics: Geology, v. 23, no. 5, p. 447–450.

Tikoff, Basil, and Teyssier, Christian, 1994, Strain modeling of displacement-field partitioning in transpressional orogens: Journal of Structural Geology, v. 16, no. 11, p. 1,575–1,588.

Truskowski, C.M., Gillis, R.J., Bull, K.F., and Regan, S.P., 2024a, Major oxide and trace element analyses for rock samples from the Haines-Takshanuk Mountains-Chilkat Peninsula area STATEMAP project, Southeast Alaska: Alaska Division of Geological & Geophysical Surveys Raw Data File 2024-18, 4 p. https://doi.org/10.14509/31286

Truskowski, C.M., Walser, S.L., Larsen, M.C., Nicolazzo, J.A., Gillis, R.J., Bull, K.F., Regan, S.P., and Darrow, M.M., 2024b, Field station locations and data for the geologic map of the Haines-Takshanuk Mountains-Chilkat Peninsula area STATEMAP project, Southeast Alaska, collected 2022 and 2023: Alaska Division of Geological & Geophysical Surveys Raw Data File 2024-17, 3 p. https://doi.org/10.14509/31285

Ulusay, Resat, and Hudson, J.A., eds., 2007, The complete ISRM suggested methods for rock characterization, testing and monitoring: 1974–2006: International Society for Rock Mechanics and Rock Engineering (ISRM), 628 p.

Wilson, F.H., Hults, C.P., Mull, C.G., and Karl, S.M., comps., 2015, Geologic map of Alaska: U.S. Geological Survey Scientific Investigations Map 3340, 197 p., 2 sheets, scale 1:1,584,000.

Yehle, L.A., and Lemke, R.W., 1972, Reconnaissance engineering geology of the Skagway area, Alaska, with emphasis on evaluation of earthquake and other geologic hazards: U.S. Geological Survey Open-File Report 72-454, 108 p., 4 sheets, scale 1:96,000. https://dggs.alaska.gov/pubs/id/10971

APPENDIX A. ROCK MASS CLASSIFICATION KINEMATIC ANALYSIS

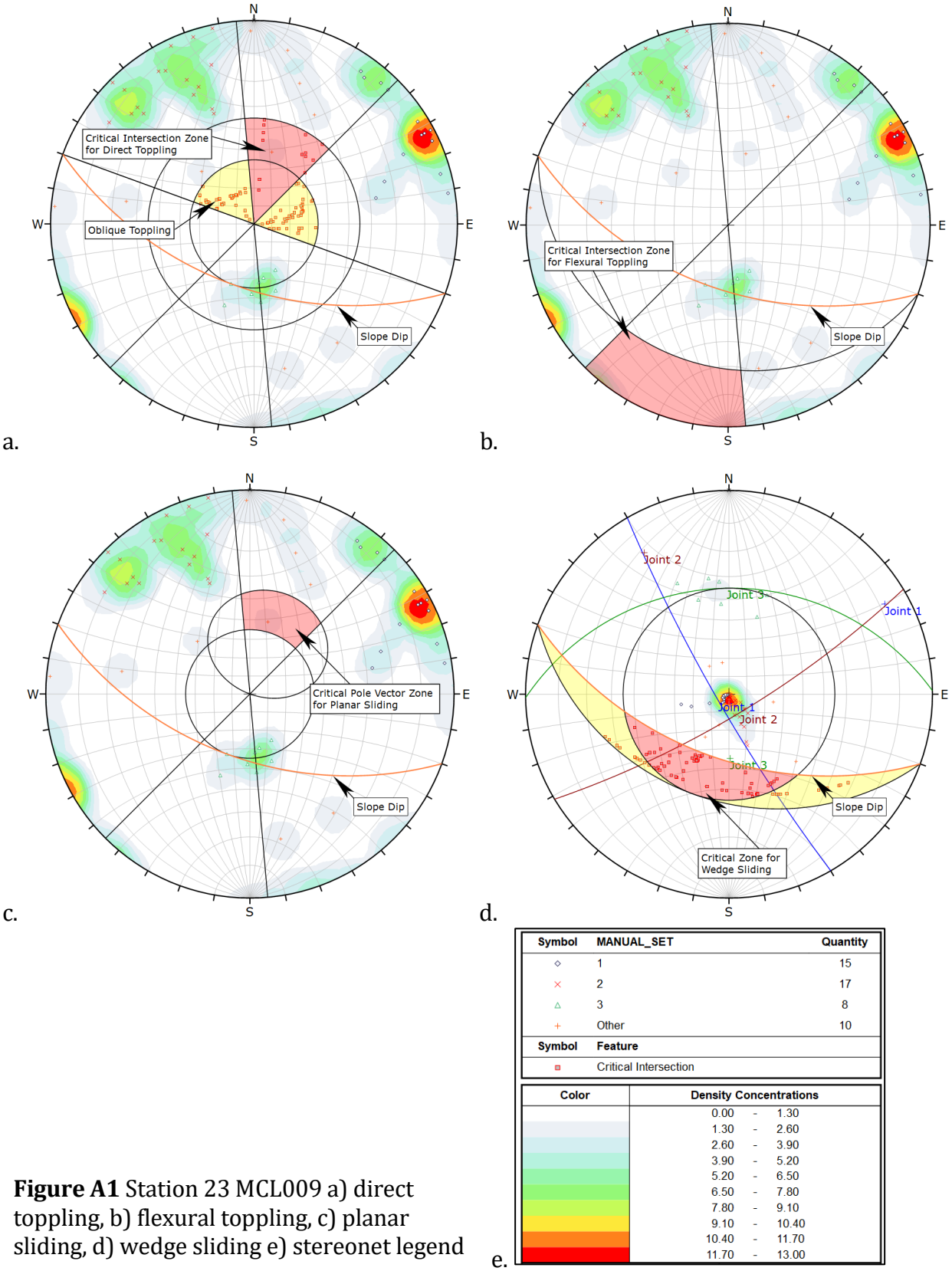

Figure A1 Station 23 MCL009 a) direct toppling, b) flexural toppling, c) planar sliding, d) wedge sliding e) stereonet legend

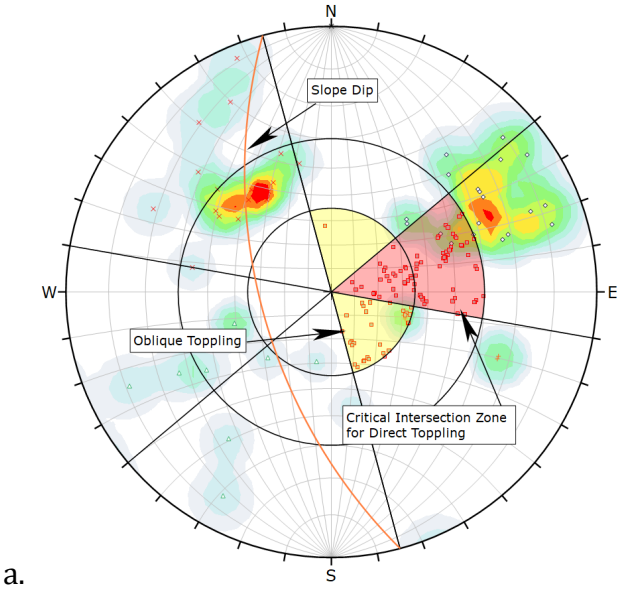

a.

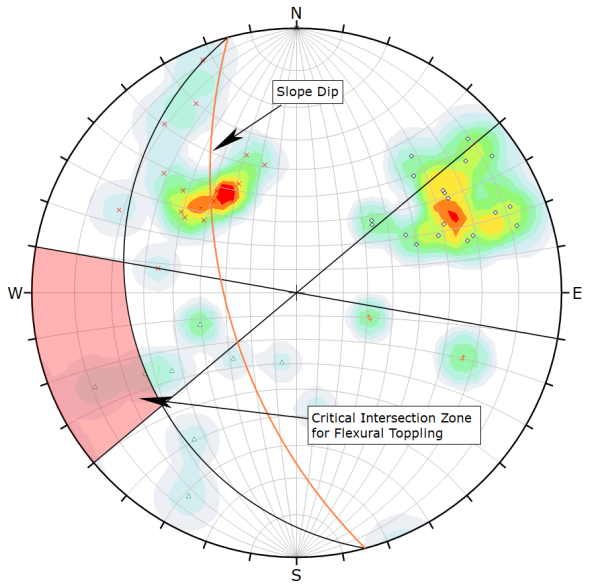

b.

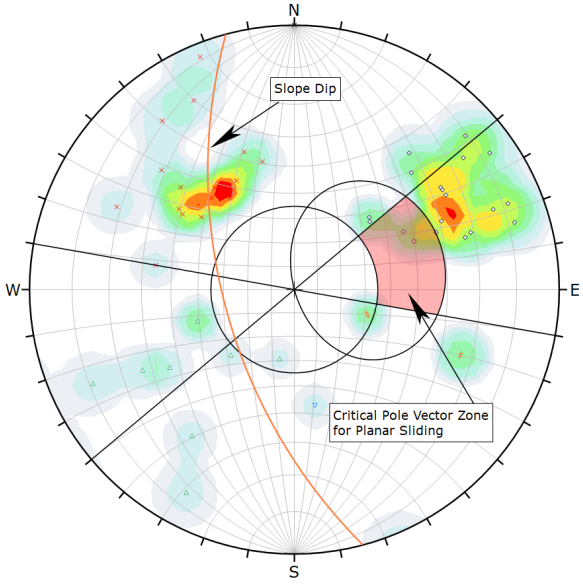

c.

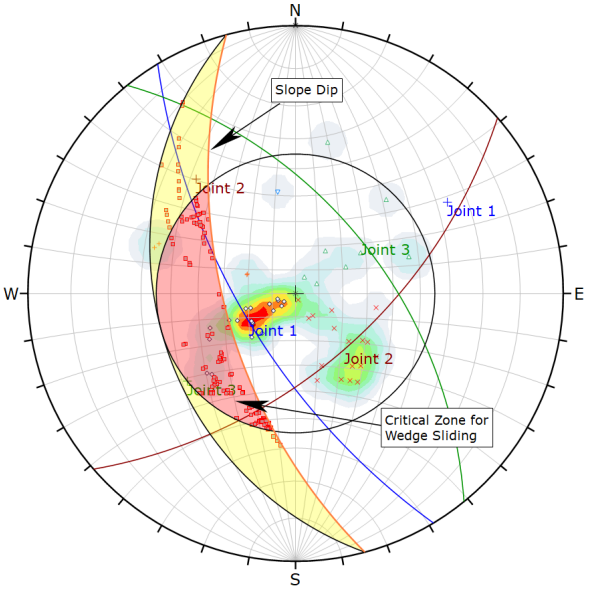

d.

Symbol	MANUAL_SET	Quantity
◇	1	19
×	2	17
△	3	9
+	Foliation	4
▽	Other	1

Symbol	Feature
▫	Critical Intersection

Color	Density Concentrations
	0.00 - 0.90
	0.90 - 1.80
	1.80 - 2.70
	2.70 - 3.60
	3.60 - 4.50
	4.50 - 5.40
	5.40 - 6.30
	6.30 - 7.20
	7.20 - 8.10
	8.10 - 9.00

e.

Figure A2 Station 23 MCL010 a) direct toppling, b) flexural toppling, c) planar sliding, d) wedge sliding e) stereonet legend

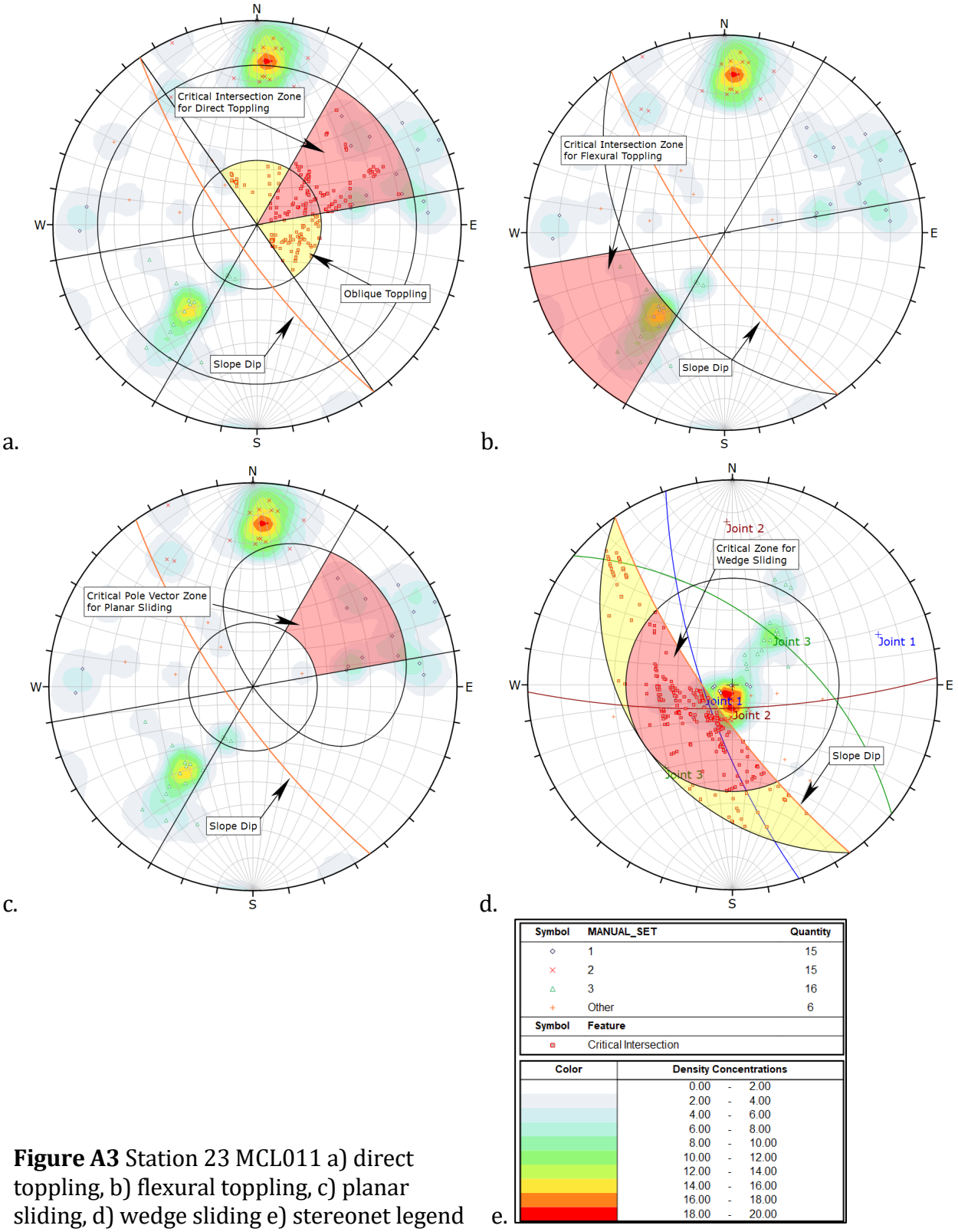

Figure A3 Station 23 MCL011 a) direct toppling, b) flexural toppling, c) planar sliding, d) wedge sliding e) stereonet legend

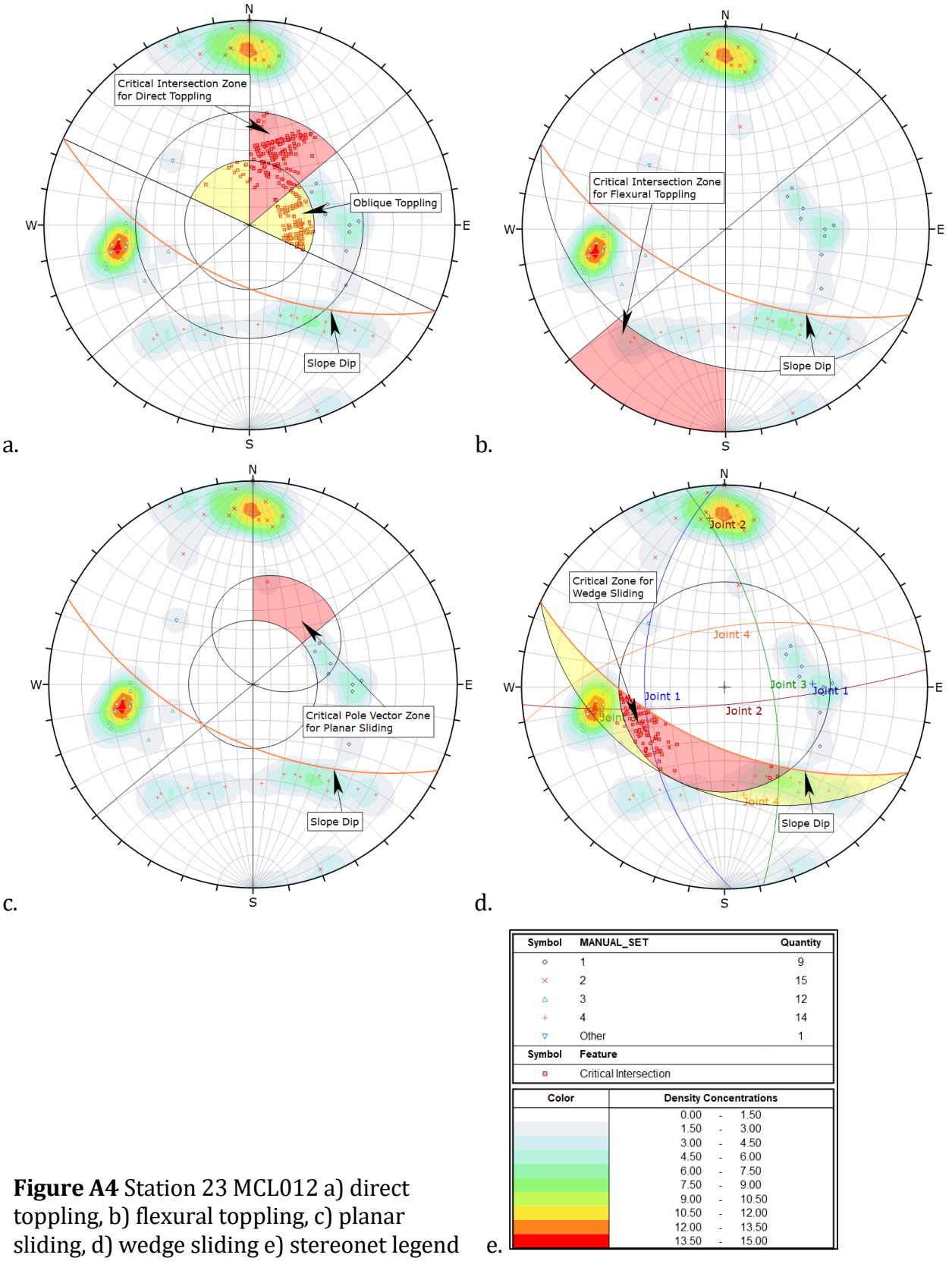

Figure A4 Station 23 MCL012 a) direct toppling, b) flexural toppling, c) planar sliding, d) wedge sliding e) stereonet legend

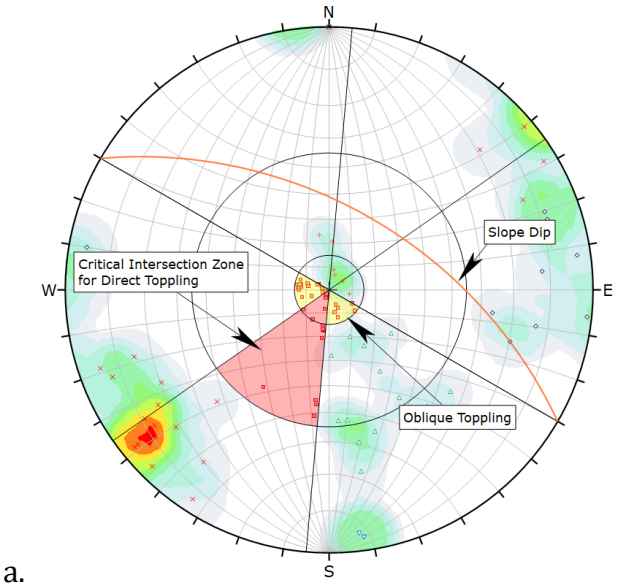

a.

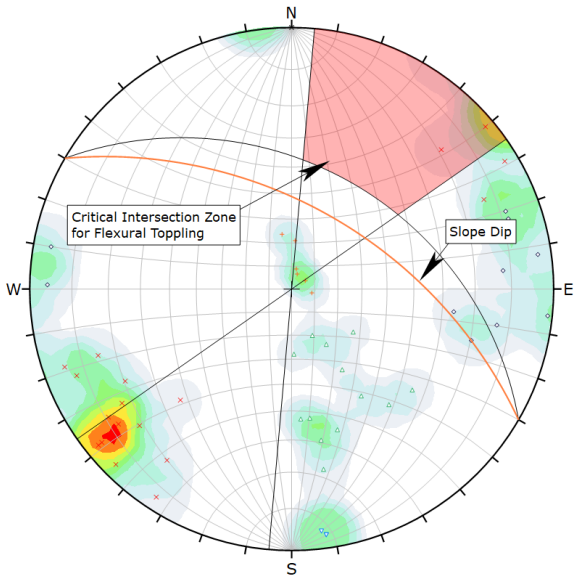

b.

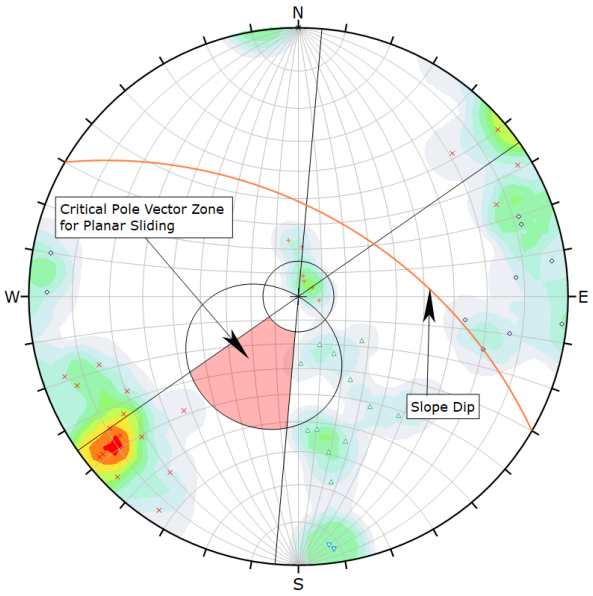

c.

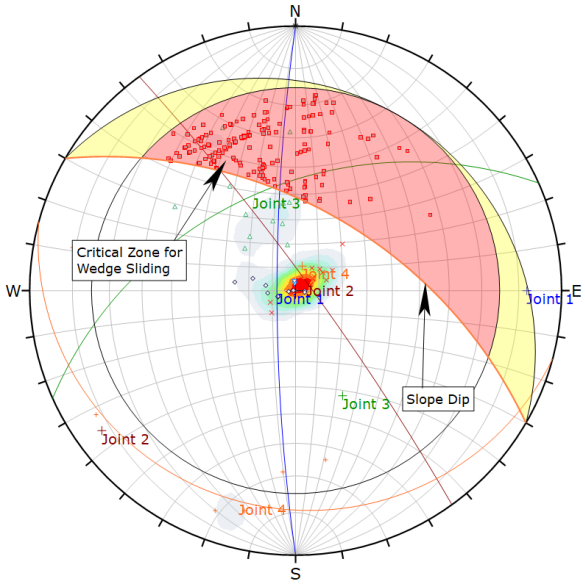

d.

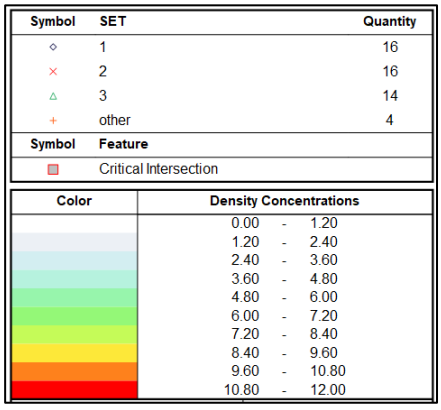

Symbol	SET	Quantity
◇	1	16
×	2	16
△	3	14
+	other	4

Symbol	Feature
▭	Critical Intersection

Color	Density Concentrations
	0.00 - 1.20
	1.20 - 2.40
	2.40 - 3.60
	3.60 - 4.80
	4.80 - 6.00
	6.00 - 7.20
	7.20 - 8.40
	8.40 - 9.60
	9.60 - 10.80
	10.80 - 12.00

e.

Figure A5 Station 23 MCL023 a) direct toppling, b) flexural toppling, c) planar sliding, d) wedge sliding e) stereonet legend